

Can the finite fracture mechanics coupled criterion be applied to V-notch tips of a quasi-brittle steel alloy?

Zohar Yosibash, Vered Mendelovich, Ilan Gilad and Arie Bussiba

Computational Mechanics and Experimental Biomechanics Lab, School of Mechanical Engineering,
Iby and Aladar Fleischman Faculty of Engineering, Tel Aviv University, Ramat Aviv 69978, Israel

May 5, 2022

Abstract

Structures made of steel alloys with V-notches may fracture at the V-notch tip at which a small plastic zone usually evolves. Failure criteria for predicting fracture loads for such quasi-brittle alloys, as a function of the V-notch opening angle are very scarce and have not been validated, to the best of our knowledge, by a set of experimental observations.

Herein we provide a database of experiments performed on AISI 4340 steel alloy specimens with three different V-notch opening angles and three different tempering temperatures, loaded in mode I. Material properties, failure load and plastic area at the V-notch tip are detailed.

The experimental observations are used to investigate to which extent the finite fracture mechanics coupled criterion (FFMCC) for brittle materials may predict the failure load of quasi-brittle steel alloys, depending on the plastic zone size. Finite element analyses were used to compute the parameters required by the FFMCC. We compared the predicted versus the experimental fracture load for the different V-notch opening angles and tempering temperatures.

For small opening angles (30°) for which the plastic area is very small, the FFMCC under-predicts the fracture load by about 20% which is within the experimental error range. The under-prediction of the failure load constantly increases to $\sim 50\%$ as the V-notch angle increases to 90° and plastic zone area increases to $\sim 0.5 \text{ mm}^2$ (for a V-notch depth of 5 mm).

The detailed experimental database is suggested to be used for validation purposes when new failure criteria for quasi-brittle materials are developed.

1 Introduction

Sharp notches in structures undergoing small strains and displacements may result in catastrophic fractures which initiate at the notch tip. Under the assumption of linear elastic fracture mechanics (LEFM) many failure criteria have been proposed that may predict the failure loads in *brittle structures* at V-notch tips, see for example [18, 10, 11, 7, 25]. Among these criteria, the finite fracture mechanics coupled criterion (FFMCC) has been largely validated by experimental observations: i.e. predicted fracture loads for different V-notch opening angles and different brittle materials closely matched the experimental data for simplified boundary conditions which excite symmetric opening of notch faces (mode I loading) [11, 25, 2]. An overview of the FFMCC for brittle materials is given in [23]. Since in practice most of these V-notched tips are not sharp but are rounded (a small radius at the V-notch tip), correction factors were introduced in [13] which allowed to adjust the predicted fracture load as a function of the V-notch tip radius. It is worth mentioning that the FFMCC has been extended to mixed mode I/II loadings, see e.g. [15, 26, 17] and also to three dimensional domains with mixed mode I/II/III loadings [24, 3]. In these three-dimensional cases the vertex-edge intersection is of particular interest, see e.g. for brittle materials [28].

In engineering practice many structures are made of steel alloys which have a small plastic zone at the V-notch tip, depending on the V-notch angle and material properties. In such cases, the amount of strain energy dissipated by the creation of the plastic zone increases as the plastic zone increases and the failure criteria's prediction accuracy monotonically decreases. Various elasto-plastic failure criteria have been proposed to predict the fracture load due to V-notches [29, 8, 6, 16, 20, 12, 22, 9, 21], some of which are for ductile materials. However, most require complex computational resources and none have been validated by a systematic experimental investigation.

It is therefore of major engineering importance to carefully quantify to which extent the FFMCC for brittle materials can accurately predict the fracture load in steel alloys structures as a function of the generated plastic zone prior to fracture. To the best of the authors' knowledge such a quantification has never been performed, and an experimental database for V-notches under an increased zone of plastic strain in the vicinity of V-notch tips is unavailable.

We present herein a careful experimental protocol on AISI 4340 steel alloy specimens. We determined the elasto-plastic material properties, the fracture toughness, and assessed the plastic zone and fracture load in specimens with three different V-notch opening angles. We chose to

investigate AISI 4340 for its popularity and the possibility to perform different thermal procedures so to obtain different G_{Ic} and different σ_y . In addition to the failure load we measured by digital image correlation also the plastic zone developed prior to failure at the V-notch tips of a large set of specimens (55 specimens). This database is presented herein and used to check to which extent can the FFMCC, developed for brittle materials, predict the failure load.

In Section 2 we report the experiments performed to determine material properties of AISI 4340 steel alloy in different tempering conditions. In this chapter experiments performed for determination of Young's modulus E , yield and ultimate stress and strains $\sigma_y, \sigma_{uts}, \varepsilon_y, \varepsilon_{uts}$ and fracture toughness K_{Ic} are presented. Section 3 presents the V-notch specimens, experimental methods and specimens dimensions. Also, we describe the digital image correlation (DIC) procedure used to determine plastic zone at the free surface.

In Section 4 we briefly describe the FFMCC and collect the necessary data for its use for the prediction of the fracture load for the specimens. The computed (predicted) failure load is thereafter compared to the experimental measured one. The plastic zone area is thereafter discussed in Section 5 - we summarize the measured plastic zone area at the V-notch tip. We then detail the finite element (FE) analyses performed to estimate the plastic area and compare it to the experimental observations. Both linear elastic and elasto-plastic FEA were performed showing that the area obtained by the linear elastic FEA is a good approximation to the elasto-plastic FEA plastic zone.

Summary and conclusions are discussed in Section 6.

Appendices (supplementary material) detail tensile experiments, fracture toughness experiments, dimensions of all specimens and failure loads, the V-notch diameter and plastic zone area measured by DIC.

2 Experiments to determine material properties of AISI 4340 in different tempering conditions

To represent a range of K_{Ic} and σ_y we used specimens with four different tempering temperature. Material's mechanical properties were determined by 8 tension specimens of a 6.2 mm diameter (see Appendix A). The experiments to determine material's properties were performed according to ASTM E8 – 13a [4] using a MTS machine. Using VIC-3D DIC, strain as a function of time was

measured. We matched the DIC’s last photo before break and force at break so force as function of computed strain was obtained which allowed to generate the stress-strain curves.

All specimens (including the V-notched specimens) are manufactured from AISI 4340 steel alloy circular rods that were originally manufactured by extrusion. This assures that material properties have no preferred directionality in their cross-section. All manufactured specimens were vacuum-quenched and cooled by hydrogen gas, then divided into three groups each tempered by a different temperature (150, 170 and 250°C). The different tempering temperatures were chosen in an attempt to obtain specimens with different yield and ultimate stress. Material properties for 210°C tempering conditions were also evaluated but we observed no change in material properties between 210 and 250°C, so it was decided not to temper V-notched specimens at 210°C/

2.1 Mechanical properties

Circular section specimens were used for the determination of Young’s modulus, yield stress and yield strain (see details in Appendix A). These are summarized in Table 1. Young’s modulus was determined by the curve slope in the linear part. The yield stress was set according to 0.2% plastic strain offset, whereas the yield strain is the strain value at yield stress.

Table 1: Material properties for the specimens in this research.

Tempering Temp [°C]	E [GPa]	σ_y [MPa]	ε_y [strain]	σ_{uts} [MPa]	ε_{uts} [strain]	Plastic elongation [strain]
150	188	1370	0.0093	2134	0.0490	0.0375
170	188	1510	0.0100	2062	0.0587	0.0970
	192	1440	0.0095	2070	0.0580	0.0860
250	192	1500	0.0098	1812	0.0362	0.0960

2.2 LEFM properties

K_{Ic} was determined by specimens of $13mm \times 8mm$ (see Appendix B) as shown in Figure 1 and summarized in Table 2. Experiments to determine K_{Ic} were performed according to ASTM E399 – 20 [1]. The displacements were measured by a crack opening displacement (COD) gauge connected to an Instron machine. The forces and displacements were recorded by the Instron machine. K_{Ic} values were calculated according to ASTM E399 – 20.

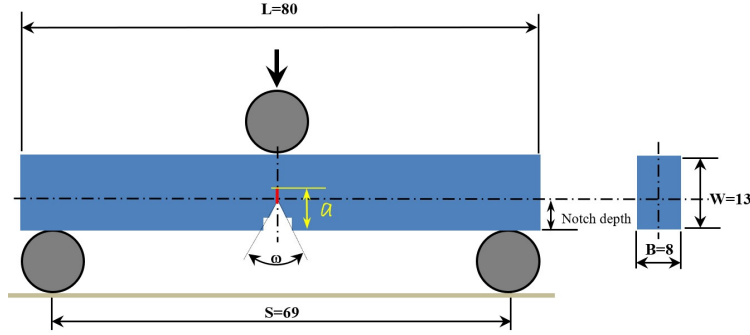


Figure 1: Specimens for K_{Ic} determination (dimensions in mm).

Table 2: Summary on K_{Ic} , and G_{Ic} .

Temp [$^{\circ}$ C]	K_{Ic} (STD) [MPa \sqrt{m}]	E [GPa]	G_{Ic} [Joul/m 2] (STD)
150	44.28 (1.58)	188	9490 (700)
170	44.75 (2.96)	188	9690 (1330)
170	44.75 (2.96)	192	9490 (1330)
250	39.74 (one specimen only)	192	7490

Inspecting Table 2 one may notice that there is no significant difference in K_{Ic} values, and one may conclude that K_{Ic} does not change much as a function of the tempering temperature. Since some of the specimens had a slightly tilted initial crack, K_{Ic} was computed also by FEA, showing a negligible change of less than 2.5

Table 21 presents K_{Ic} values obtained by our experiments using ASTM E399 - 20 and K_{Ic} values from literature [14]. One may notice for the almost same σ_y the K_{Ic} values obtained by our experiments are lower than the ones in the literature. This is attributed to the quality of the AISI 4340 steel alloy. We performed a careful heat treatment of another specimen for determination of K_{Ic} which resulted in same values.

3 V-notched specimens

Experiments on V-notched AISI 4340 steel alloys specimens are detailed herein.

A set of 55 specimens were manufactured and tested in a four-point-bending (4PB) configuration having three V-notch opening angles of 30° , 60° and 90° , as shown in Figure 2. Details on the exact dimensions of each specimen and load to fracture are tabulated in Appendix C in Tables 22-23. DIC measurements were performed at the V-notch tip area.

Typical intact and broken V-notched specimens are shown in Figure 3, (notice that these spec-

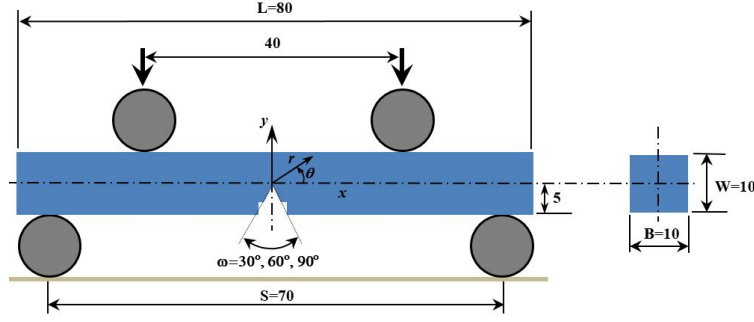


Figure 2: V-notch specimens' dimensions (in mm).

imens are of different dimensions compared to Figure 1).



Figure 3: Typical fractured specimens with (left to right) 90°, 60° and 30° V-notch angles.

The side of each specimen in the vicinity of the V-notch tip was colored in a black and white pattern for DIC measurements. Specimens were loaded in a 4PB configuration in a Shimadzu AG-IC machine (200kN maximum load) at a displacement rate of 2 mm/min. The force and stroke data were collected with a Vishay data acquisition logger (model 7000-32-SM). To prevent specimen's movement some of the specimens were held in place during the first 1000-2000N load. The 4PB experimental setup is shown in Figure 4 and in Table 8 we summarize the average measured fracture load $F_c^{experimental}$.

Figure 5 presents the fracture force as a function of the tempering temperature and notch angle. Tempering type 1, 2, 3 represent 150, 170, 250°C, respectively.

No significant difference in fracture load (F_c) is noticed in the 30° specimens for the different tempering temperature. This may be caused by the small V-notch angle, the very small plastic area, and the similar K_{Ic} values for the different tempering temperatures. The average V-notch radius increases slightly as the V-notch angle increases.

The specimens' notch tip radius is detailed in Table 3 and in Appendix D. To characterize the notch radius size of the specimens we used a microscope. For each batch and V-notch angle the first and the last specimen's radii were measured so they represent all specimens in that range.

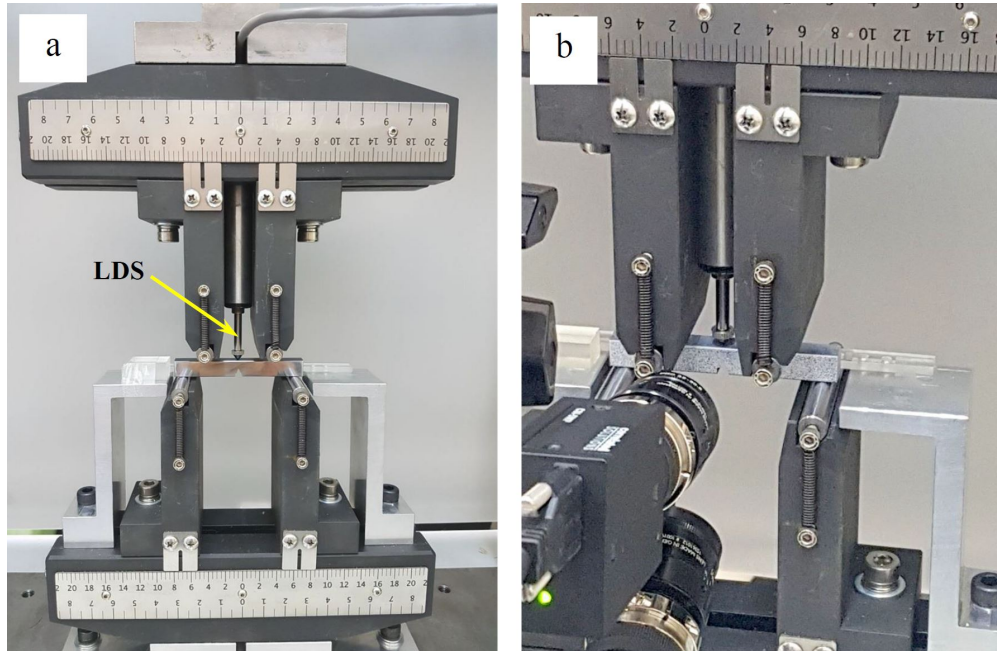


Figure 4: Experiment setup. a) Specimen in 4PB configuration, b) Stained specimen and DIC's cameras.

Table 3: Specimens' notch radius.

V-notch angle [°]	Specimen #	Specimen's side	Notch radius [μm]	Average Notch radius [μm]
30	1	A	35	41
		B	41	
	54	A	44	
		B	44	
60	2	A	40	46
		B	41	
	36	A	55	
		B	47	
90	1	A	64	69
		B	77	
	55	A	68	
		B	67	

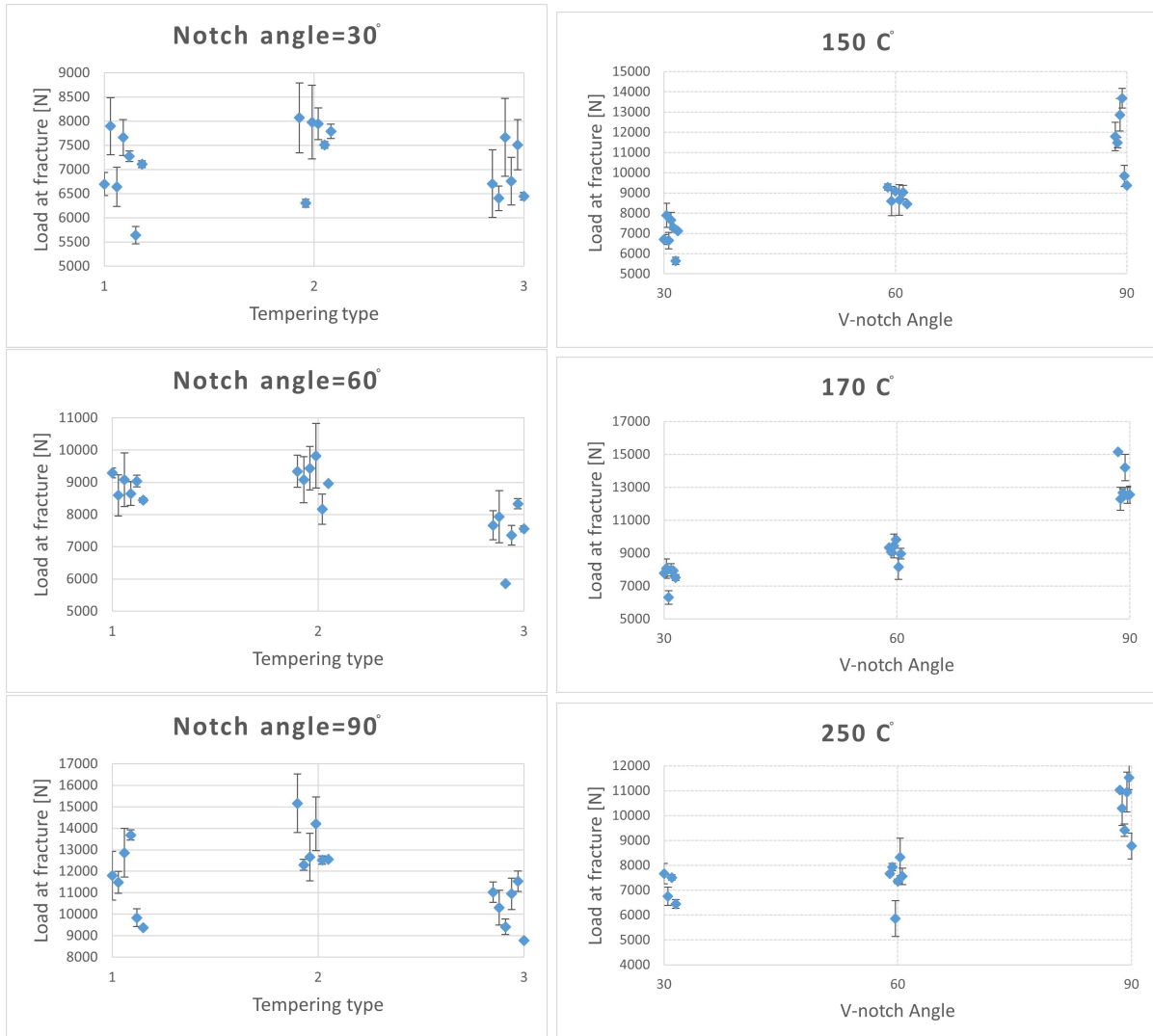


Figure 5: Fracture load as a function of the tempering type (Left Column) and notch angle (Right Column). Note that scale changes in the different graphs.

4 Predicting the fracture load by the FFMCC criterion

For a brittle material, the finite fracture mechanics coupled criterion (FFMCC) at a sharp V-notch [11] predicts the load which induces fracture, and thereafter it is adjusted according to the rounded tip by the algorithm presented in [13]. The FFMCC is based on the instantaneous fulfilment of the Griffith energy criterion and stress criterion at a given virtual distance ℓ_0 from the notch tip.

4.1 The LEFM solution in the vicinity of a V-notch

In view of the notations in Figure 2, the displacements in the vicinity of the V-notch tip under mode I may be expressed by the generalized stress intensity factor A_1 (GSIF), and the eigen-displacements:

$$u_x = A_1 r^{\alpha_1} s_x^{(1)}(\theta) + \mathcal{O}(r), \quad u_y = A_1 r^{\alpha_1} s_y^{(1)}(\theta) + \mathcal{O}(r) \quad (1)$$

and the stress component σ_{xx} for example may be computed by the GSIFs and the eigen-stress $S_{xx}^{(1)}(\theta)$:

$$\sigma_{xx} = A_1 r^{\alpha_1 - 1} S_{xx}^{(1)}(\theta) + \mathcal{O}(1) \quad (2)$$

where the eigenvalue α_1 is the solution to:

$$\sin(\alpha_1 \omega^*) + \alpha_1 \sin(\omega^*) = 0 \quad (3)$$

and $\omega^* = 2\pi - \omega$. For the three V-notch angles of interest: $\alpha_1(30^\circ) = 0.5014530$, $\alpha_1(60^\circ) = 0.5122214$, $\alpha_1(90^\circ) = 0.5444837$.

The GSIF A_1 and the eigen-displacements can be computed by high order finite element methods with high accuracy [27]. A_1 depends linearly on the applied load, but the the eigen-displacements and eigen-stresses depend only on the V-notch angle and material properties. $S_{xx}^{(1)}(\theta)$ is computed from (1):

$$S_{xx}^{(1)}(\theta) = \frac{E}{(1+\nu)(1-2\nu)} \left[(1-\nu) \frac{\partial u_x}{\partial x} + \nu \frac{\partial u_y}{\partial y} \right] \quad (4)$$

$u_x(r, \theta)$ and $u_y(r, \theta)$ being functions of r, θ , the derivatives in Cartesian coordinates are evaluated by derivatives in cylindrical coordinates:

$$\frac{\partial u_x}{\partial x} = \left[\cos \theta \frac{\partial}{\partial r} - \frac{\sin \theta}{r} \frac{\partial}{\partial \theta} \right] u_x, \quad \frac{\partial u_y}{\partial y} = \left[\sin \theta \frac{\partial}{\partial r} + \frac{\cos \theta}{r} \frac{\partial}{\partial \theta} \right] u_y \quad (5)$$

Substituting (1) & (5) in (4) one obtains $S_{xx}^{(1)}$ at $\theta = \pi/2$:

$$S_{xx}^{(1)}(\pi/2) = \frac{E}{(1+\nu)(1-2\nu)} \left[(\nu-1) \frac{\partial s_x^{(1)}(\pi/2)}{\partial \theta} + \nu \alpha_1 s_y^{(1)}(\pi/2) \right] \quad (6)$$

$\frac{\partial s_x^{(1)}(\theta)}{\partial \theta}$ in (5) is computed using five-points midpoint formula [5].

4.2 The FFMCC for sharp V-notches

The FFMCC predicts fracture under the critical load denoted by F_c which in turn induces the critical GSIF $A_1^c \times S_{xx}^{(1)}(\pi/2)$ [11], that is equal to the value determined by the fracture toughness and critical stress:

$$A_1^c \times S_{xx}^{(1)}(\pi/2) = \left(\frac{G_{Ic}}{K(\omega)} \right)^{1-\alpha_1} \sigma_c^{2\alpha_1-1} \quad (7)$$

$K(\omega)$ depends on the local geometry and boundary conditions in the vicinity of the V-notch tip and computed in [26]. $K(\omega)$ also depends on Young modulus and Poisson's ratio and is given for AISI 4340 in Table 4:

Table 4: Values of $K(\omega)$ as function of E and notch angle.

E [GPa]	$K(\omega) \left[\frac{1}{MPa} \right]$		
	30°	60°	90°
188	0.00002999	0.00002895	0.00002602
192	0.00002936	0.00002834	0.00002548

Since the FFMCC considers a linear elastic material one may compute $A_1^{(1N)} S_{xx}^{(1)}(\pi/2)$ for a 1 N load and then multiply it by F_c to compute A_1^c :

$$A_1^c \times S_{xx}^{(1)}(\pi/2) = F_c \times A_1^{(1N)} \times S_{xx}^{(1)}(\pi/2). \quad (8)$$

Substituting (8) in (7) FFMCC predicts the failure load F_c by:

$$F_c = \frac{\left(\frac{G_{Ic}}{K(\omega)} \right)^{1-\alpha_1} \sigma_c^{2\alpha_1-1}}{A_1^{(1N)} S_{xx}^{(1)}(\pi/2)} \quad (9)$$

G_{Ic} is the surface energy release rate which is obtained for plane strain by:

$$G_{Ic} = \frac{K_{Ic}^2}{E/(1-\nu^2)} \quad (10)$$

Remark 4.1 For a non-brittle material one may use for σ_c either σ_y or σ_{uts} . Both options will be used in the sequel.

Remark 4.2 The increase in F_c as the V-notch opening angle ω increases is proportional to σ_c and inversely proportional to K_{Ic} . I.e. in view of (9), the ratio $F_c(\omega_2)/F_c(\omega_1)$ for $\omega_2 > \omega_1$:

$$\frac{F_c(\omega_2)}{F_c(\omega_1)} = \left[\frac{\sigma_c^2}{G_{Ic}} \right]^{\alpha_1(\omega_2) - \alpha_1(\omega_1)} \frac{(K(\omega_1))^{1-\alpha_1(\omega_1)} A_1^{(1N)}(\omega_1) S_{xx}^{(1)}(\omega_1)(\theta = \pi/2)}{(K(\omega_2))^{1-\alpha_1(\omega_2)} A_1^{(1N)}(\omega_2) S_{xx}^{(1)}(\omega_2)(\theta = \pi/2)} \quad (11)$$

increases as σ_c increases and K_{Ic} decreases. The lower the K_{Ic} and the higher the σ_c , the more steep will be the increase of the failure load as the V-notch angle is increasing.

For example, Alumina-Zirconia and PMMA, are brittle materials having a relatively small K_{Ic} .

For

Alumina-Zirconia $K_{Ic}=4.1 \text{ MPa } \sqrt{\text{m}}$, $\sigma_c = 290 \text{ GPa}$ and for

PMMA $K_{Ic}=1.03 \text{ MPa } \sqrt{\text{m}}$, $\sigma_c = 124 \text{ GPa}$, and $K(\omega)$ for both are reported in [25]. Thus,

AISI 4340 $K_{Ic} \sim 44 \text{ MPa } \sqrt{\text{m}}$, $\sigma_c \sim 2000 \text{ GPa}$

for Alumina-Zirconia: $\frac{F_c(60^\circ)}{F_c(30^\circ)} = 1.04$ and $\frac{F_c(90^\circ)}{F_c(30^\circ)} = 1.16$ and for

PMMA $\frac{F_c(60^\circ)}{F_c(30^\circ)} = 1.05$ and $\frac{F_c(90^\circ)}{F_c(30^\circ)} = 1.19$

AISI 4340 $\frac{F_c(60^\circ)}{F_c(30^\circ)} = 1.04$ and $\frac{F_c(90^\circ)}{F_c(30^\circ)} = 1.10$

In former publications the FFMCC was validated by experiments on brittle materials with relatively small K_{Ic} so that the increase in the failure load of about 20% could be noticed as ω was increased from 30° to 90° for example. Herein, we show that for materials with a high K_{Ic} ($\sim 40 \text{ MPa } \sqrt{\text{m}}$), the increase in failure load is less than half.

After we obtain F_c^{computed} we compare this value to $F_c^{\text{experimental}}$ to check if the brittle criterion is valid for all V-notch angles and if there is an upper limit of the plastic zone area so the criterion is not valid anymore. Because the criterion's validity depends on the plastic zone area, we compute and measure the plastic area for the specimens by experiments and finite element analysis in the next Section.

For the FFMCC criterion to be valid, the virtual crack length ℓ_0 has to be small relative to the characteristic length of the structure [11]. ℓ_0 , depends on σ_c , G_{Ic} and $K(\omega)$:

$$\ell_0 = \frac{G_{Ic}}{K(\omega)\sigma_c^2} \quad (12)$$

G_{Ic} in Table 2, σ_y or σ_{uts} in Table 15, and $K(\omega)$ in Table 4 are used to estimate ℓ_0 and F_c by the FFMCC. ℓ_0 computed by (12) is presented in Table 5.

Table 5: Values of ℓ_0 .

	σ_c [MPa]	Tempering temperature [°C]	E [MPa]	ℓ_0 [mm]		
				30°	60°	90°
$\sigma_c = \sigma_y$	1370	150	188000	0.17	0.17	0.19
	1510	170		0.14	0.15	0.16
	1440	170	192000	0.16	0.16	0.18
	1500	250		0.11	0.12	0.13
$\sigma_c = \sigma_{uts}$	2134	150	188000	0.07	0.07	0.08
	2062	170		0.08	0.08	0.09
	2070	170	192000	0.08	0.08	0.09
	1812	250		0.08	0.08	0.09

ℓ_0 obtained by $\sigma_c = \sigma_{uts}$ are a bit smaller than the results obtained using $\sigma_c = \sigma_y$ and in both cases ℓ_0 is 25 to 75 times smaller than the V-notch depth.

We compute $A_1^{(1N)} S_{xx}^{(1)}(\pi/2)$ at the middle of the specimen by high-order finite element (FE) methods using a 3D linear elastic model at the middle of the specimen, under a load of 1 N. The FE models are shown in the next Section. To ensure the correctness of $A_1^{(1N)}$ and $S_{xx}^{(1)}$ we computed the displacements u_x and u_y in the vicinity of a V-notch tip for mode I loading by (1) and compare these to the FEA results in Table 6 (computations are at $r = 2$ mm and $\theta = 0^\circ$). An excellent match can be noticed.

The values $A_1^{(1N)} S_{xx}^{(1)}(\pi/2)$ for the various V-notched specimens are summarized in Table 7 for a force of 1 N.

The predicted F_c assuming a sharp V-notch in a brittle material is obtained using (9) and summarized is in Table 8. A very small difference is noticed if one use $\sigma_c = \sigma_{uts}$ or $\sigma_c = \sigma_y$.

Table 6: Displacements' comparison using 3D FEA and equation (1).

V-Notch angle	FEA - 3D		By (1)	
	u_x	u_y	u_x	u_y
30°	-8.860e-02	-4.335e-01	-8.88E-02	-4.38E-01
60°	-1.270e-01	-6.211e-01	-1.27E-01	-6.28E-01
90°	-1.379e-01	-6.687e-01	-1.37E-01	-6.76E-01

Table 7: $A_1^{(1N)} S_{xx}^{(1)}(\pi/2)$ [MPa mm $^{(1-\alpha_1)}$] for a force of 1N.

V-Notch angle	E=188 [GPa]		E=192 [GPa]	
	T=150°C	T=170°C	T=170°C	T=250°C
30°	0.1071	0.1071	0.1071	0.1071
60°	0.1081	0.1081	0.1081	0.1081
90°	0.1140	0.1140	0.1140	0.1140

4.3 The influence of the V-notch tip radius on the predicted fracture load

The predicted fracture load under the assumption of a sharp V-notch can be corrected for brittle materials to adjust the influence a rounded V-notch, given that the radius is at the same order as ℓ_0 . The V-notch average tip radii range from 40 μm for the 30° V-notch to 70 μm for the 90° V-notch (see Table 3), whereas ℓ_0 is between 70 μm and 200 μm (see Table 5), i.e. of similar order. In view of the small notch tip radius we assume that a correction factor of the same magnitude as in [13] can be applied (ignoring the plasticity effects, so to comply with the simplified assumption of an almost brittle material), where correction factors for two brittle materials are provided. AISI 4340 has a higher yield stress and G_{Ic} compared to Alumina-Zirconia reported in [13] (~ 1500 MPa compared to 290 MPa, and ~ 9500 J/m 2 compared to 45 J/m 2), and of course is a semi-brittle material, but it is assumed that the order of the percentage of the correction factors are similar: for a 40-60 μm V-notch tip radii the correction is about 4% for the 30° notch, about 7% for the 60° notch and about 10% for the 90° notch.

A graphical representation of the predicted fracture load after adjusting for the rounded V-notch tip, compared to the average measured one, as the V-notch angle is increased, is shown in Figure 6.

Failure load is under-predicted compared to the experimental observations where only for the

Table 8: Predicted fracture load $F_c^{computed}$ by G_{Ic} and σ_c ([Newtons]), and the experimental average $F_c^{Experimental}$.

V-Notch angle	E [GPa]	T [$^{\circ}C$]	$F_c^{computed}$ [N]		$F_c^{Experimental} \pm \text{STD}$ [N]
			$\sigma_c = \sigma_y$	$\sigma_c = \sigma_{uts}$	
30 $^{\circ}$	188	150	5268	5274	6990\pm752
		170	5324	5329	7598\pm 665
	192	170	5324	5330	
		250	4732	4735	6914\pm 542
60 $^{\circ}$	188	150	5412	5471	8850\pm 1334
		170	5481	5523	9136\pm 562
	192	170	5473	5522	
		250	4882	4904	7451\pm 849
90 $^{\circ}$	188	150	5698	5927	11503\pm 2673
		170	5802	5965	13232\pm 1171
	192	170	5778	5968	
		250	5206	5295	10332\pm 1054

30° V-notch it is within the error bar of the experimental observation. The relative difference between average experimental failure load and the predicted ones are summarized in Table 9.

Table 9: Percent of underestimation of the fracture load compared to average experimental observations.

Temp °C	V-notch angle		
	30°	60°	90°
150	21%	34%	45%
170	27%	36%	53%
250	29%	30%	44%

The difference increases as the V-notch angle increases, and corresponds to the increase in the plastic area at the V-notch tip as documented in next section. The difference between the predicted and experimental failure load for the 30° V-notch, although the plastic area is small, can be explained by the inaccurate rounded notch tip correction factor, the existence of a plastic zone (although small) and slight underestimation of the fracture toughness K_{Ic} .

The monotonic increase in the plastic zone area at the V-notch tip as the V-notch angle increases results in an increase in the difference between the brittle FFMCC and experimental observations (this plastic zone dissipates strain energy as being formed and enlarged).

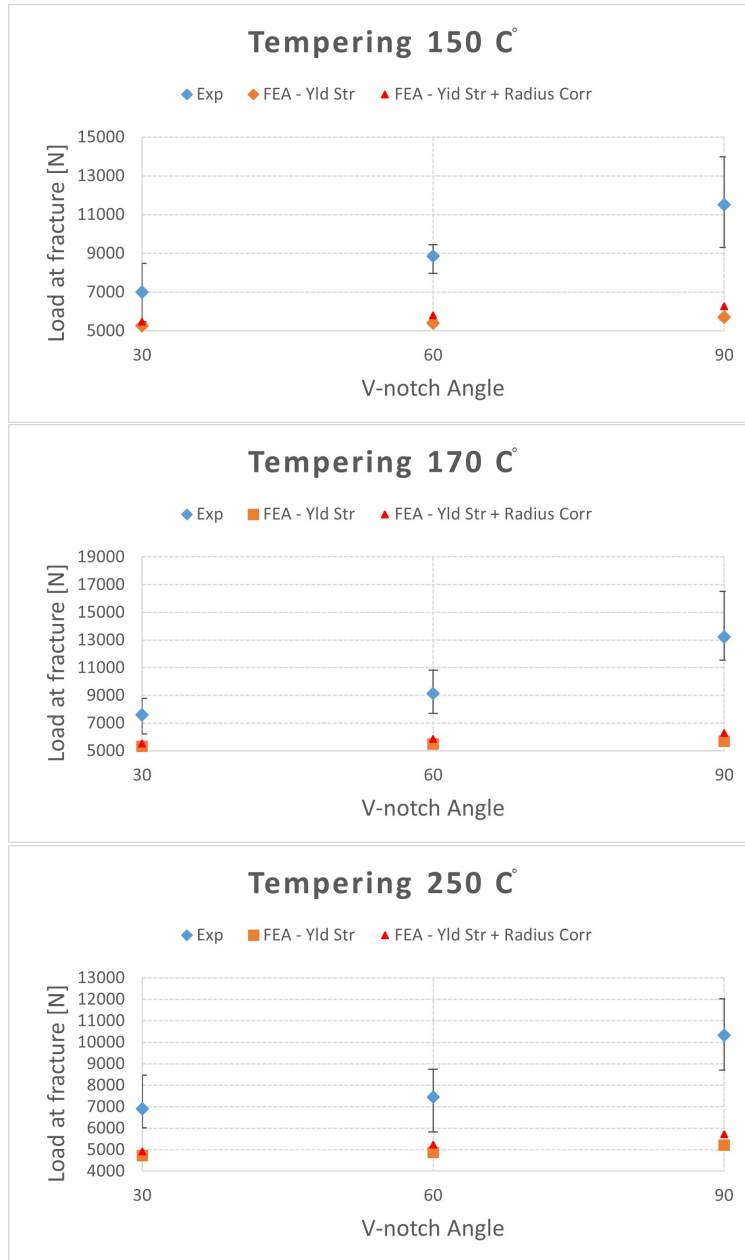


Figure 6: Predicted (using $\sigma_c = \sigma_y$) vs experimental fracture load for the three V-notch angles. The experimental average and min and max experimental values as error bars.

5 The plastic zone in the vicinity of V-notch tip

To determine plastic zone area in the experiments, we used DIC (digital image correlation) and VIC-3D software¹. The DIC system includes two 5.0-megapixel digital cameras at 30 frames per second with a Schneider Xenoplan 1.9/35mm lens for the first 12 specimens and a Schneider Xenoplan 1.4/17mm lens for the rest of the specimens. Surface specimen's deformation in the vicinity of the V-notch tip during the experiments were recorded and processed by VIC-3D. The equivalent strain for each specimen was computed and the plastic zone was defined as the area at which $\varepsilon_{eq} > \varepsilon_y$.

Since surface strains are recorded, a plane stress condition was assumed so the equivalent strain is computed by:

$$\varepsilon_{eq} = \sqrt{\frac{1}{2(1+\nu)^2} [(\varepsilon_1 - \varepsilon_2)^2 + (\varepsilon_2 - \varepsilon_3)^2 + (\varepsilon_3 - \varepsilon_1)^2]} \quad (13)$$

For a 1D tensile, $\varepsilon_2 = \varepsilon_3 = -\nu\varepsilon_1$, (13) results in: $\varepsilon_{eq} = \varepsilon_1$.

By assuming $\nu = 0.5$, (13) becomes the well known ε_{eq} in plasticity:

$$\varepsilon_{eq} = \sqrt{\frac{2}{9} [(\varepsilon_1 - \varepsilon_2)^2 + (\varepsilon_2 - \varepsilon_3)^2 + (\varepsilon_3 - \varepsilon_1)^2]} \quad (14)$$

Otherwise, if an elastic assumption is made then:

$$\varepsilon_{eq} = \sqrt{\frac{1}{(1-\nu^2)^2} [(1-\nu+\nu^2)(\varepsilon_1^2 + \varepsilon_2^2) + \varepsilon_1\varepsilon_2 \times (4\nu-1-\nu^2)]} \quad (15)$$

We use (15) to compute the equivalent strain from DIC data. For AISI 4340 $\nu = 0.3$, and for plastic behavior $\nu \approx 0.5$. The stress-strain curves show a plastic strain which is not negligible relative to the total strain, which is the summation of the plastic strain and elastic strain. Since DIC recorded strain cannot be divided into elastic and plastic parts, we cannot determine what Poisson's ratio is, but it is bounded by 0.3 and 0.5. Therefore, all the results from DIC uses both $\nu = 0.3$ and 0.5 to present the range of the actual plastic zone.

The plastic zones on specimens are given in Appendix E - blue represents the elastic zone, and cyan represents the plastic zone. In the grey areas, VIC-3D cannot calculate ε_{eq} either due to low speckle quality, or along a V-notch's boundary. Figure 7 presents an example of a plastic zone. The plastic area was computed by drawing a curve in Maya² software on the cyan outer boundary.

¹VIC-3D is a trademark of Correlated Solution Incorporated, USA.

²Maya is a trademark of Autodesk, 111 McInnis Parkway San Rafael, 94903 California, U.S.

The curve includes the “grey holes” on the cyan surface. Plastic areas are presented in Tables 36-38 in Appendix E (reported areas include the grey holes and grey area at V-notch faces).

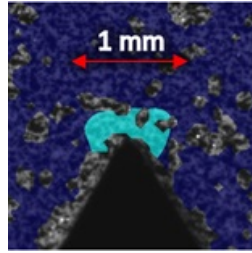


Figure 7: An example of plastic zone determined by DIC (plastic zone colored by cyan).

The small area along V-notch edges at which the DIC data cannot compute strains is termed threshold area. Figure 9 presents an example of a specimen which may contain a plastic zone in the threshold area. Table 10 presents the threshold area (the minimum plastic zone area being possible to identify by DIC’s resolution), calculated by an average of the threshold areas for each notch angle.

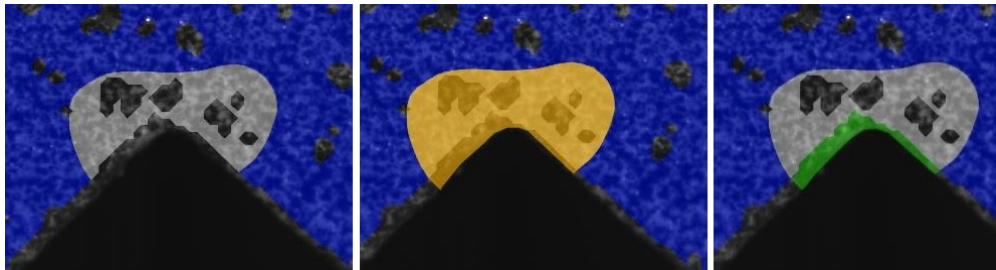


Figure 8: From left: An original photo, plastic zone (in yellow) and a threshold area (in green).

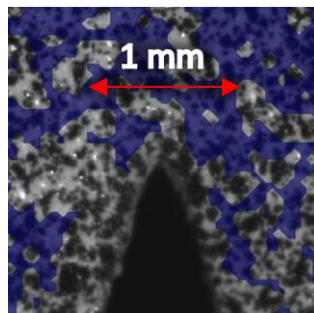


Figure 9: An example of a specimen which may contain a plastic zone in threshold area.

Figure 10 presents graphically the plastic zone area as function of the notch angle and tempering temperatures.

The tempering temperature has little influence on the plastic zone. This is also manifested

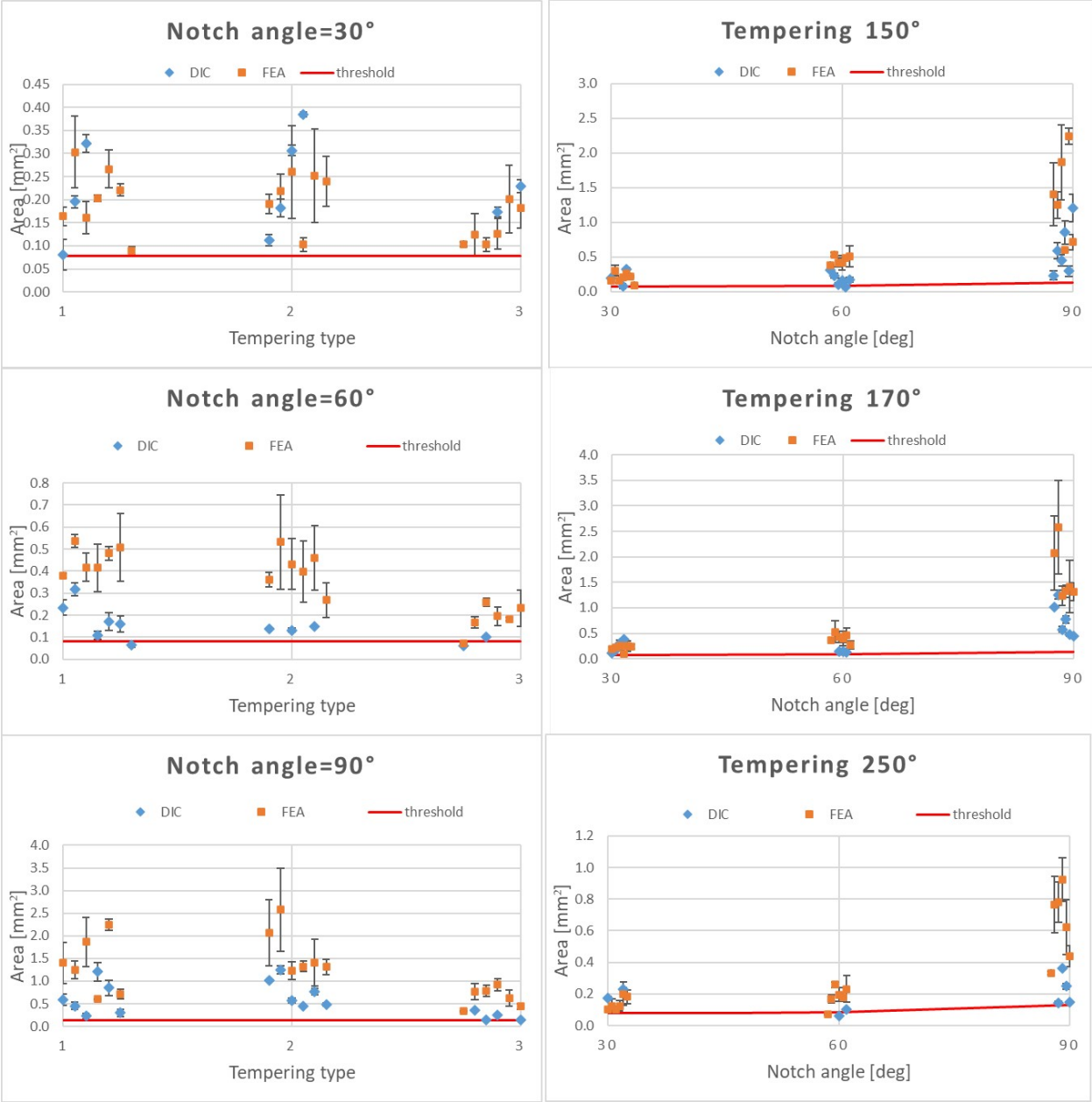


Figure 10: Plastic zone area as a function of the notch angle and tempering temperature (DIC measurements & FE estimation based on plane stress).

Table 10: Threshold plastic area for each notch angle.

Notch angle [°]	Threshold area[mm ²]
30	0.0782
60	0.0825
90	0.1315

in the minor difference in σ_y between specimens of different tempering temperature. The 250°C specimens have a smaller plastic zone for all V-notch angles.

Generally, a small increase in plastic zone area is noticed between 30° to 60° and a more pronounced plastic zone area increase is noticed between 60° to 90°. No much difference is observed between the plastic area obtained for 30° and 60° angles.

5.1 Computing the plastic zone area by FEA

To investigate how well the elastic FEA estimates the plastic zone, so to determine what is the plastic area above which the brittle FFMCC’s predictions are deteriorating, a linear finite element analysis of all specimens was performed by the high order FEA code StressCheck³. Two dimensional models with E taken from the tension experiment results and $\nu = 0.3$ were created. A four-bend-point loading was applied as in the experiment with a plane stress situation because it resembles the stress state on the specimen’s surface. The critical load at fracture in experiments was applied in the FEA. In Figure 11 the FE models of the three experimental configurations are shown. The mesh was graded in a geometrical progression towards the V-notch tip with the smallest element at the tip of dimension of 2 μm . Displacement boundary conditions $u_x = u_y = 0$ were applied in the right support and $u_y = 0$ was applied on the left support. Distributed load was applied on 2 edges at the top of the FE model. The FEA was performed for polynomial degrees 1 to 8, monitoring the convergence in energy norm to have a relative error of less than 5.5%.

Strains and stresses were computed by StressCheck and saved in a file. The plastic zone (for example as shown in Figure 18) was obtained by using Maya on the strains and stresses saved in these files. Maya is a graphical software so the calculation of the plastic zone area is almost immediate. The principal stresses $\sigma_1, \sigma_2, \sigma_3$ computed by the FEA were used in (16) to determine

³StressCheck is a trademark of ESRD, St. Louis, MO, USA.

σ_{eq} . The approximated plastic zone area determined by the FEA is compared to the plastic zone obtained by DIC, to check the prediction of the plastic zone dimensions by the FEA.

$$\sigma_{eq} = \sqrt{\frac{1}{2} \left[(\sigma_1 - \sigma_2)^2 + (\sigma_2)^2 + (\sigma_1)^2 \right]} = \sqrt{\sigma_1^2 + \sigma_2^2 - \sigma_1 \sigma_2} \quad (16)$$

Yielding is determined either by $\sigma_{eq} > \sigma_y$ or by $\varepsilon_{eq} > \varepsilon_y$.

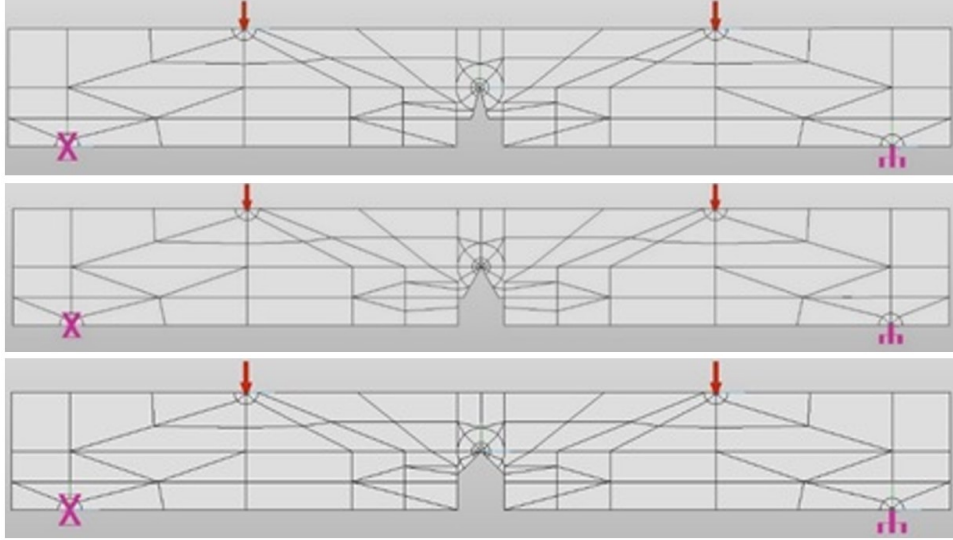


Figure 11: FE meshes with $\omega = 30^\circ, 60^\circ, 90^\circ$ (top to bottom) respectively.

The linear FEA plastic zone predicted by $\varepsilon_{eq} > \varepsilon_y$ is of different dimensions compared to the plastic zone predicted by $\sigma_{eq} > \sigma_y$. The “actual plastic zone” is best computed by an elasto-plastic analysis. We also performed an elasto-plastic analysis using the Ramberg-Osgood’s constitutive model [19], which is characterized by four parameters: E, ν , the stress (S_{70E}), which is the stress corresponding to the intersection of the stress-strain curve with a line which passes through the origin and has the slope of $0.70E$, and the hardening exponent n :

$$\varepsilon = \frac{\sigma}{E} + \frac{3}{7} \frac{S_{70E}}{E} \left(\frac{\sigma}{S_{70E}} \right)^n \quad (17)$$

The two different plastic zones computed by the linear elastic FEA, determined by either $\sigma_{eq} > \sigma_y$ or $\varepsilon_{eq} > \varepsilon_y$, and the plastic zones obtained by the elasto-plastic (EP) analysis are compared to DIC measurements in Table 11. The comparison is for three typical specimens with different V-notch angles and tempering temperatures. For the linear FEA a different plastic zone is predicted using σ_{eq} or ε_{eq} , which is not the case for the elasto-plastic analysis.

Table 11: Plastic zone area comparison using FEA (red) and DIC (cyan).

Specimen / criterion	FEA – Elastic - σ_{eq}	FEA – Elastic - ϵ_{eq}	FEA – EP - σ_{eq}	FEA – EP - ϵ_{eq}	DIC- ϵ_{eq}
$\omega = 30^\circ$ $T = 150^\circ\text{C}$ $\sigma_y = 1370\text{MPa}$ $\epsilon_y = 0.93\%$					
$\omega = 60^\circ$ $T = 170^\circ\text{C}$ $\sigma_y = 1440\text{MPa}$ $\epsilon_y = 0.95\%$					
$\omega = 90^\circ$ $T = 250^\circ\text{C}$ $\sigma_y = 1500\text{MPa}$ $\epsilon_y = 0.98\%$					

The dimensions of the plastic zone area in the elastic FEA, using **equivalent stress** criterion, are similar to the dimensions obtained by the EP analysis. *We therefore use the equivalent stress to determine the plastic zone area by a linear elastic FEA and compare it to the DIC measurements.* This plastic zone area is a good measure for the energy dissipated to create the plastic area (or volume).

The plastic zone areas for all specimens are summarized in Tables 36-38 in Appendix E and graphically presented in Figure 10. We present the plane stress results because it mostly resembles the DIC results on specimen's surface and the EP FEA. In the FEA $F_c^{experimental}$ was applied as load boundary condition of each specimen. A summary of plastic zone areas computed and measured is provided in Table 12 and plotted in Figure 12.

One may conclude that plastic zone area using the EP FEA is well described by the elastic FEA, using equivalent stress criterion. For all V-notch angles the plastic zone area obtained both by DIC and FEA does not change as function of the tempering temperature which is also manifested in the minor difference in σ_y . A small increase in plastic zone area is noticed between 30° and 60° and a more pronounced plastic zone area increase is noticed between 60° and 90° . The plastic zone is

Table 12: Comparison between measured plastic zone area and linear elastic FEA. Average and standard deviation in mm^2 .

	150°C		170°C		250°C	
V-notch Angle	DIC	FEA	DIC	FEA	DIC	FEA
30°	0.16 ±0.13	0.20 ±0.07	0.25 ±0.12	0.21 ±0.06	0.14 ±0.10	0.14 ±0.04
60°	0.18 ±0.09	0.46 ±0.06	0.14 ±0.01	0.41 ±0.09	0.08 ±0.03	0.18 ±0.06
90°	0.60 ±0.37	1.35 ±0.64	0.76 ±0.32	1.66 ±0.54	0.23 ±0.10	0.64 ±0.22

reasonably well represented by the linear elastic FEA for the 30° V-notched specimens and provides a good estimate of the growing plastic zone as the V-notch angle increases.

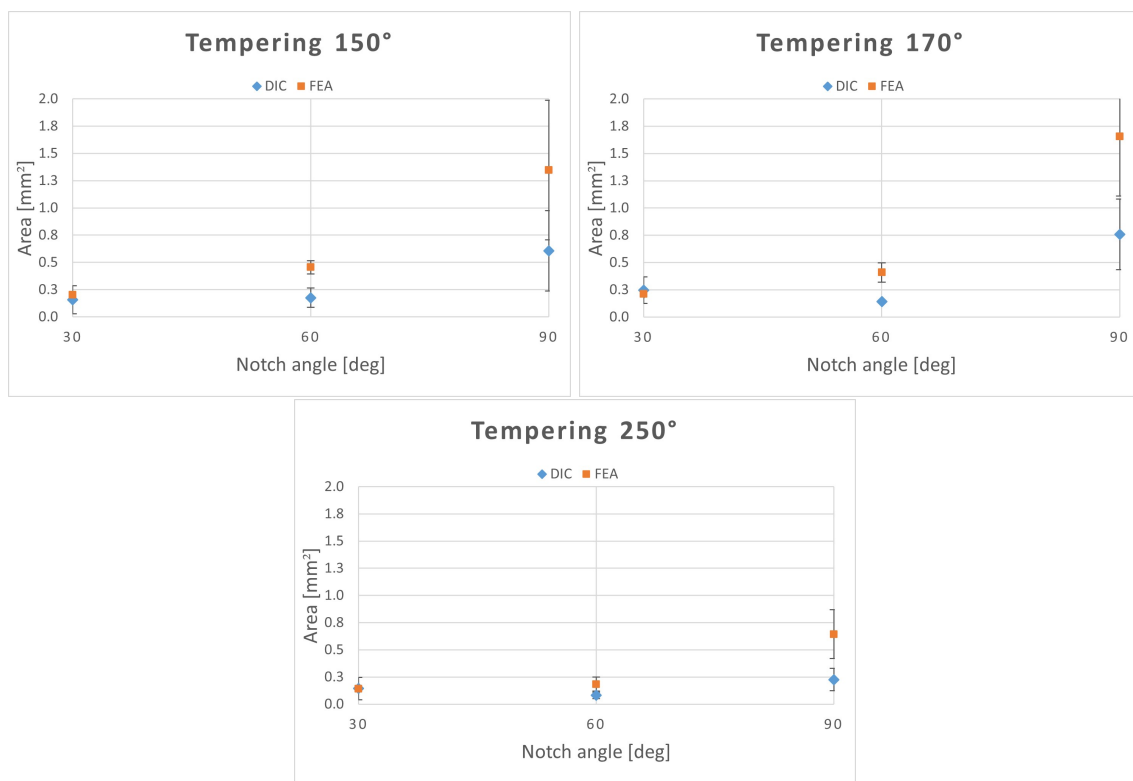


Figure 12: Average plastic zone areas computed by linear elastic FEA and measured by DIC for 150, 170 and 250°C specimens

Plane stress situation better represents the specimen's surface, however the plastic zone inside the specimen is better represented by a plane strain situation. In Table 13 we present the plastic zone area computed by linear FEA using plane-stress and plane-strain based on equivalent stress. The fracture occurs in the middle of the specimen, which is best represented by plane strain. One may clearly observe the smaller plastic zone in the specimen itself, and in Table 14 the ratio between the areas of plane stress and plane strain for each notch angle is summarized.

Table 13: Plastic zones area computed by a plane stress and plane strain FEA for each notch angle (σ_{eq} criterion, elastic analysis).

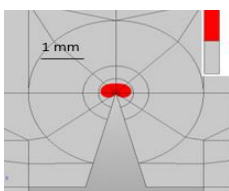
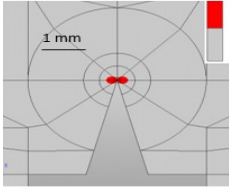
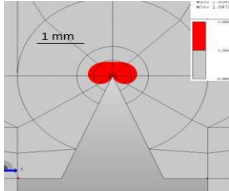
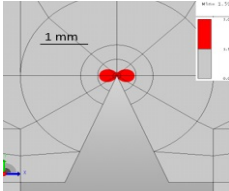
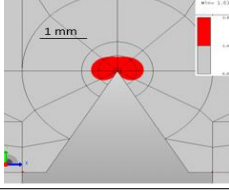
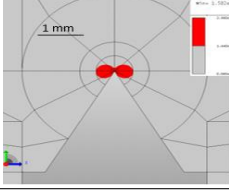
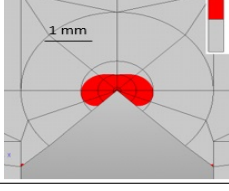
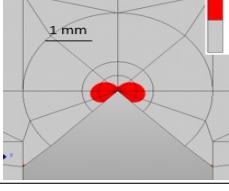
Specimen	σ_{eq} - plane stress	σ_{eq} - plane strain
$\omega = 30^\circ$ $T = 150^\circ C$ $\sigma_y = 1370 MPa$		
$\omega = 45^\circ$ $T = 250^\circ C$ $\sigma_y = 1500 MPa$		
$\omega = 60^\circ$ $T = 170^\circ C$ $\sigma_y = 1440 MPa$		
$\omega = 90^\circ$ $T = 250^\circ$ $\sigma_y = 1500$		

Table 14: Plastic zone area comparison: plane-stress vs plane-strain ($\sigma_{eq} > \sigma_y$ criterion).

Notch angle	Area [mm ²]		Plane strain/ plane stress Area [%]
	Plane stress	Plane strain	
30°	0.2247	0.0771	34.31
60°	0.5398	0.2151	39.85
90°	0.9055	0.4332	47.84

One may conclude that although we measured and computed the plastic zone area on the specimens' surface, in most of the specimen's V-notch edge, the plastic zone is smaller by about twice for 90° notch angle and gets even smaller to one third for the 30° notch angle - i.e. making it of an order of 0.05 mm² for the 30° V-notched specimens and increasing to about 0.4 mm² for the 90° specimens.

6 Summary and Conclusions

Failure load and plastic zone generated at the V-notch tip of a popular high strength steel alloy, AISI 4340, were measured on 55 specimens having three different V-notch opening angles. The database was used to quantifying to which extent can the FFMCC, developed for brittle materials, predict the failure load. To the best of the authors' knowledge such a quantification has never been performed, and the experimental database provides the means to validate other proposed failure criteria.

We found that predicted failure load is almost independent whether one uses σ_y or σ_{uts} as the critical stress σ_c in the FFMCC. This is because even for the largest V-notch angle 90° the singularity exponent is slightly different than 1/2 and critical stress is not affecting much the computation of the failure load. The virtual crack ℓ_0 was found to be ≈ 0.07 to 0.2 mm which is much smaller than specimens's V-notch dimensions, thus the assumption for the asymptotic expansion (based on which FFMCC was developed) is still considered to be valid.

The FFMCC for brittle materials underestimates the failure load by 21-29 % for 30° V-notch angle, and the underestimation increases monotonically to 44-53 % for 90° V-notch angle. This is a large underestimation compared to former experiments performed on brittle materials. Comparing to Alumina-7%Zirconia and PMMA [25, 13] the difference between $F_c^{Experimental}$ and $F_c^{Computed}$ after correction of the tip radius is:

	Alumina-7%Zirconia	PMMA	AISI 4340
30°	~9% difference		21-29 %
60°	~7% difference	2%	30-36 %
90°	~10% difference	8%	44-53 %

We conclude that for crack openings of 30° and below, and a plastic zone of less than 0.25 mm²,

it is useful to use the brittle version of FFMCC, predicting an underestimation of the failure load by about 20%.

The predicted increase in fracture load from a V-notch angle of 30° to 60° is about 3% and from 30° to 90° is 8%. This small change is caused by the high K_{Ic} and the moderate σ_y, σ_{uts} (see remark 4.2). The actual change in failure load is by far more dramatic in experiments - attributed to an increase in the plastic zone area (*but may also indicate on a possible deterioration in the predicability of the brittle FFMCC for high toughness materials*) - this topic has to be further investigated in future experiments on high toughness brittle materials.

Although a slight increase in σ_y and σ_{uts} of the specimens as the tempering temperature increased from 150°C to 250°C , the K_{Ic} did not change much, thus the fracture loads did not differ much for specimens with same V-notch angles undergoing different tempering temperatures.

The value of K_{Ic} was lower by about 20% compared to similar materials in the literature - after a fractographic examination of the fracture surface, the lower value was attributed to the low quality of material's batch. This low quality of the material and imperfections in the shape and dimensions of the tip radii are assumed to be another reasons for the scatter in the fracture loads.

The estimated plastic zone area computed by a simplified linear elastic FEA and equivalent plastic stress, when compared to the elasto-plastic FEA and experimental observations showed a good correlation. The plastic zone in the elasto-plastic FEA seems to be rounded in its shape and a bit different than the plane strain shape. DIC was used successfully to determine the small scale yielding plastic area in the vicinity of the V-notch tip - to the best of our knowledge this is the first manuscript that provides these plastic zones ahead of V-notched tips just before fracture.

The recently developed quasi-brittle FFMCC in [12] will be investigated (in a follow-up manuscript) whether it can better predict failure loads for such steels with V-notches having a V-notch angle larger than 30° .

Acknowledgements

The authors gratefully acknowledge the support by the Israel Science Foundation (grant No. 964/18) which made this research possible.

References

- [1] ASTM E399 – 20. Standard test method for linear-elastic plane-strain fracture toughness of metallic materials.
- [2] P. Cornetti, N. Pugno, A. Carpinteri, and D. Taylor. Finite fracture mechanics: A coupled stress and energy failure criterion. *Engrg. Frac. Mech.*, 73:2021–2033, 2006.
- [3] A. Doitrand and D. Leguillon. 3D application of the coupled criterion to crack initiation prediction in epoxy/aluminum specimens under four point bending. *Int. J. Solids and Structures*, 143:175–182, 2018.
- [4] ASTM E8-13a. Standard test methods for tension testing of metallic materials.
- [5] Rachid Fakir, Nouredine Barka, and Jean Brousseau. Mechanical properties analysis of 4340 steel specimen heat treated in oven and quenching in three different fluids. *Metals and Materials International*, 24(5):981–991, 2018.
- [6] RC Flicek, DA Hills, and D Dini. Refinements in the characterisation of mode-mixity and small scale yielding at sharp notch roots. *Engrg. Frac. Mech.*, 126:73–86, 2014.
- [7] FJ Gómez and M Elices. Fracture of components with v-shaped notches. *Engrg. Frac. Mech.*, 70(14):1913–1927, 2003.
- [8] DA Hills and D Dini. Characteristics of the process zone at sharp notch roots. *Int. J. Solids and Structures*, 48(14-15):2177–2183, 2011.
- [9] VD Kurguzov and AV Shutov. Elasto-plastic fracture criterion for structural components with sharp V-shaped notches. *Int. J. Fracture*, 228(2):179–197, 2021.
- [10] Paolo Lazzarin and R Zambardi. A finite-volume-energy based approach to predict the static and fatigue behavior of components with sharp v-shaped notches. *Int. J. Fracture*, 112(3): 275–298, 2001.
- [11] D Leguillon. Strength or toughness? A criterion for crack onset at a notch. *Eur. Jour. Mech. A - Solids*, 21(1):61–72, 2002.
- [12] D. Leguillon and Z. Yosibash. Failure initiation at V-notch tips in quasi-brittle materials. *Int. J. Solids and Structures*, 122–123:1–13, 2017.

- [13] Dominique Leguillon and Zohar Yosibash. Crack onset at a v-notch. influence of the notch tip radius. *Int. J. Fracture*, 122(1):1–21, 2003.
- [14] William T Matthews. Plane strain fracture toughness (kic) data handbook for metals. Technical report, ARMY MATERIALS AND MECHANICS RESEARCH CENTER WATERTOWN MA, 1973.
- [15] E. Priel, A. Bussiba, I. Gilad, and Z. Yosibash. Mixed mode failure criteria for brittle elastic V-notched structures. *Int. J. Fracture*, 144:247–265, 2007.
- [16] A. Sapora and D. Firrao. Finite fracture mechanics predictions on the apparent fracture toughness of as-quenched Charpy V-type AISI 4340 steel specimens. *Fatigue. & Frac. Eng. Mat. Struct.*, 40:949—958, 2017.
- [17] A. Sapora, P. Cornetti, and A. Carpinteri. A finite fracture mechanics approach to V-notched elements subjected to mixed-mode loading. *Engrg. Frac. Mech.*, 97:216 – 226, 2013.
- [18] Andrzej Seweryn. Brittle fracture criterion for structures with sharp notches. *Engrg. Frac. Mech.*, 47(5):673–681, 1994.
- [19] StressCheck. Master guide, release 7, august 2005.
- [20] Ali Reza Torabi. Estimation of tensile load-bearing capacity of ductile metallic materials weakened by a v-notch: The equivalent material concept. *Materials Science and Engineering: A*, 536:249–255, 2012.
- [21] Ali Reza Torabi, Filippo Berto, and Alberto Sapora. Finite fracture mechanics assessment in moderate and large scale yielding regimes. *Metals*, 9(5), 2019.
- [22] AR Torabi, A Campagnolo, and F Berto. Large-scale yielding failure prediction of notched ductile plates by means of the linear elastic notch fracture mechanics. *Strength of Materials*, 49(2):224–233, 2017.
- [23] P. Weissgraeber, D. Lequillon, and W. Becker. A review of finite fracture mechanics: crack initiation at singular and non-singular stress raisers. *Archive Applied Mechanics*, 86:375 – 401, 2016.

- [24] Z. Yosibash and B. Mittelman. A 3-D failure initiation criterion from a sharp V-notch edge in elastic brittle structures. *European J. Mech. - A/Solids*, 60:70–94, 2016.
- [25] Z. Yosibash, A. Bussiba, and I. Gilad. Failure criteria for brittle elastic materials. *Int. J. Fracture*, 125(3-4):307–333, 2004.
- [26] Z. Yosibash, E. Priel, and D. Leguillon. A failure criterion for brittle elastic materials under mixed-mode loading. *Int. J. Fracture*, 141(1):291–312, 2006.
- [27] Zohar Yosibash. *Singularities in Elliptic Boundary Value Problems and Elasticity and Their Connection with Failure Initiation*. Springer, 2012.
- [28] Behnam Zakavi, Andrei Kotousov, and Ricardo Branco. Overview of three-dimensional linear-elastic fracture mechanics. *Int. J. Fracture*, 2021. doi: 10.1007/s10704-021-00528-9.
- [29] Michele Zappalorto and Paolo Lazzarin. Strain energy-based evaluations of plastic notch stress intensity factors at pointed v-notches under tension. *Engrg. Frac. Mech.*, 78(15):2691–2706, 2011.

A Tensile Experiments

Eight cylindrical tensile specimens of 6.2 mm diameter were colored by a white color with a black speckle. Using VIC-3D DIC and an MTS tensile machine we generated the stress-strain curves. The experiments were performed according to ASTM E8 – 13a and the yield stress was set according to 0.2% offset from the linear line. The experiments were used to determine Young's modulus, yield stress and yield strain, necessary compute plastic zone dimensions for 150°, 170° and 250°C temperature specimens.

In Figure 13 specimens A.1 and A.2 broke at the radius or very close to it, so it is not clear whether the initial diameter at this section was 6.2 mm.

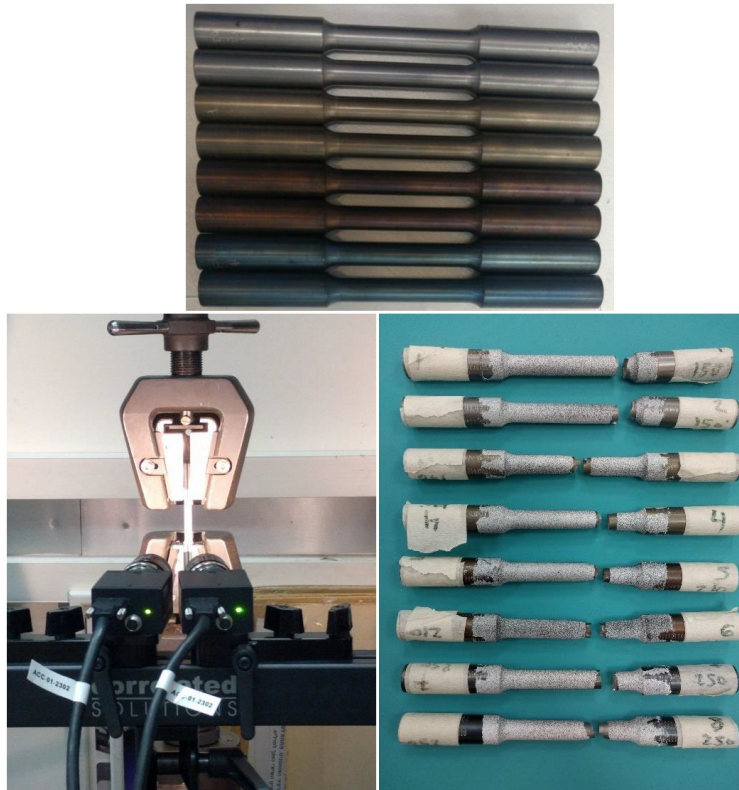


Figure 13: Specimens (top photo), the specimens in the tensile machine and after experiments (bottom photo).

Figure 14 shows the stress-strain response for each specimen and Figure 15 shows the stress-strain response for all specimens. These were generated by VIC-3D DIC and MTS output.

For specimen A.1 the measured Young's modulus and yield strain are significant higher and lower respectively to the other specimens. This may had occurred because specimen A.1 broke at the radii zone and it was hard to determine what the diameter at the broken zone was, but

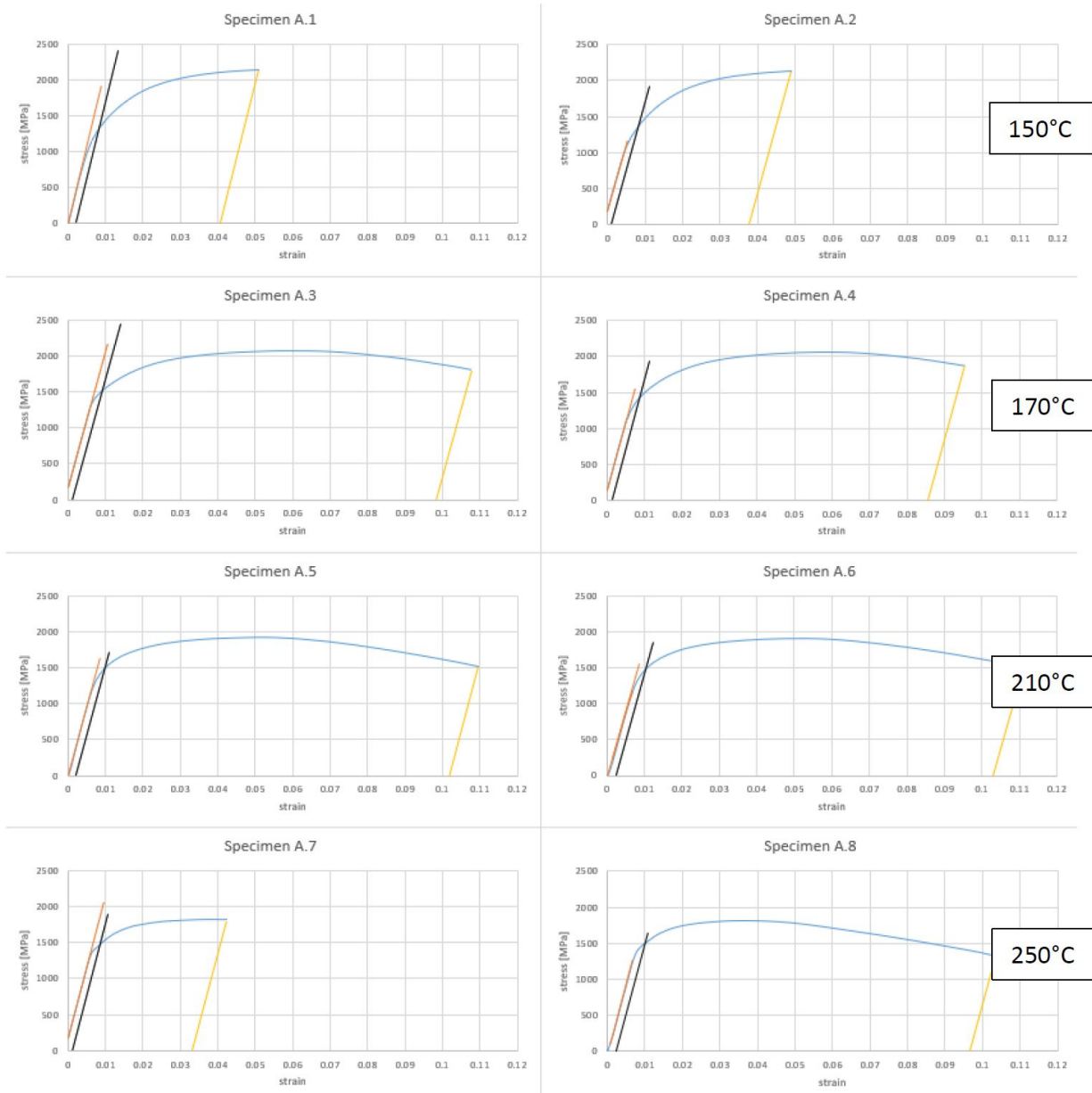


Figure 14: Stress-strain response for each specimen.

it is not 6.2 mm as the other specimens. Inspecting Young's modulus and yield strain obtained for specimen A.1 we suspect it is an outlier. Specimen A.7 has a considerable different plastic elongation compared to all other specimens, but all other values are close to specimen A.8 values. Therefore, for tempering temperature 250°C we chose to keep the data for specimen A.8. Table 15 summarizes the material properties obtained by the tensile experiments.

Figure 16 presents graphically the yield stress, yield strain, UTS stress and Young's modulus as these change as a function of the tempering temperature.

The yield stress and yield strain seem to increase as a function of the tempering temperature,

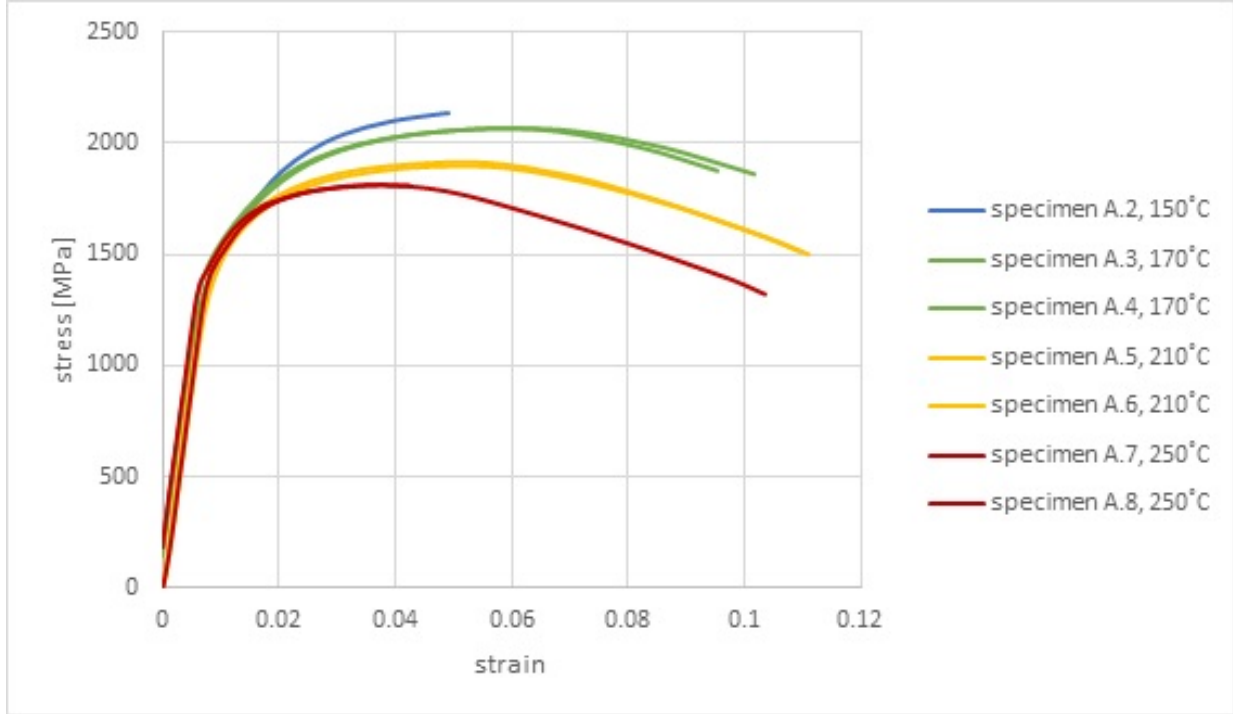


Figure 15: Stress-strain response for all specimens.

Table 15: Material properties measured by experiments.

Tempering Temp [°C]	Specimen #	E [GPa]	σ_y [MPa]	ε_y [strain]	σ_{uts} [MPa]	ε_{uts} [strain]	Plastic elongation [strain]
150	1	211	1330	0.0083	2146	0.0509	0.0410
	2	188	1370	0.0093	2134	0.0490	0.0375
170	3	188	1510	0.0100	2062	0.0587	0.0970
	4	192	1440	0.0095	2070	0.0580	0.0860
210	5	192	1490	0.0098	1920	0.0525	0.1020
	6	184	1480	0.0100	1900	0.0510	0.1025
250	7	196	1475	0.0095	1813	0.0425	0.0330
	8	192	1500	0.0098	1812	0.0362	0.0960

and the UTS stress decrease as a function of tempering temperature. The Young's modulus is almost unaffected and is about 190 GPa. σ_y & ε_y clearly increase from 150° to 170° but therefore

remain almost of the same values.

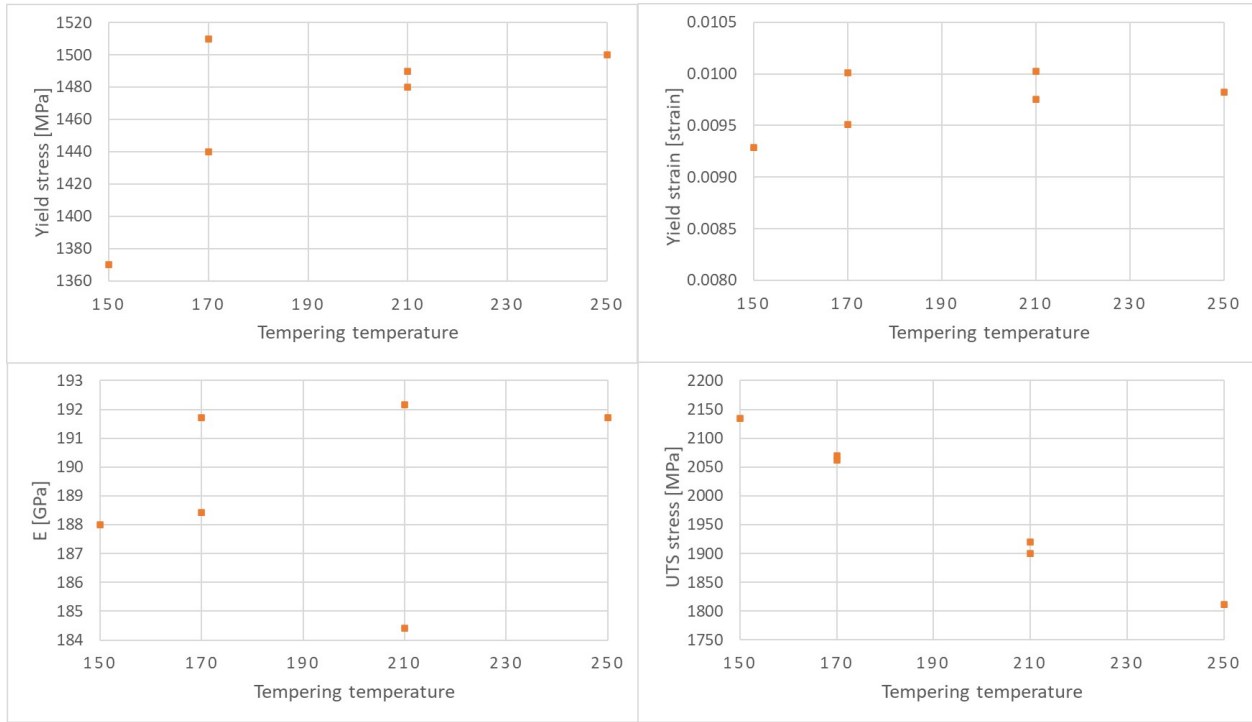


Figure 16: Yield stress, yield strain, UTS stress and Young’s modulus as a function of tempering temperature.

To confirm the mechanical properties we measured, we compared our results to properties from an article [5] which reports data on same AISI 4340 steel alloy treated by similar quenching and tempering. The data was taken from Table 2 and Figure 5a of that paper.

The three specimens in [5] were quenched and cooled in air, then they were tempered. The tempering temperature of our specimens was 250° and in [5] it was 300 degrees.

The Young’s modulus in [5] is close to our results. We see a downward tendency of the yield stress and the UTS stress as a function of the tempering temperature which means our mechanical properties are in good correspondence with [5]. We see a sharp upward tendency of the strain at fracture as a function of the tempering temperature between our results and these in [5].

Table 16: Comparison between our tensile experiments and [5].

	E [GPa]	σ_y [MPa]	ε_y [strain]	σ_{uts} [MPa]	ε_{uts} [strain]
Specimen 8	192	1500	0.0098	1812	0.0362
[5]	~200	1417	~0.0013	1552	~0.0038

B K_{Ic} experiments

The experimental setup and dimensions of a typical specimen are shown in Figure 17. In this three-point bending experiment 8 V-notches specimens were tested according to ASTM E399 – 20. In Figure 18 one may observe the P_Q determination. The blue line represents the Force –

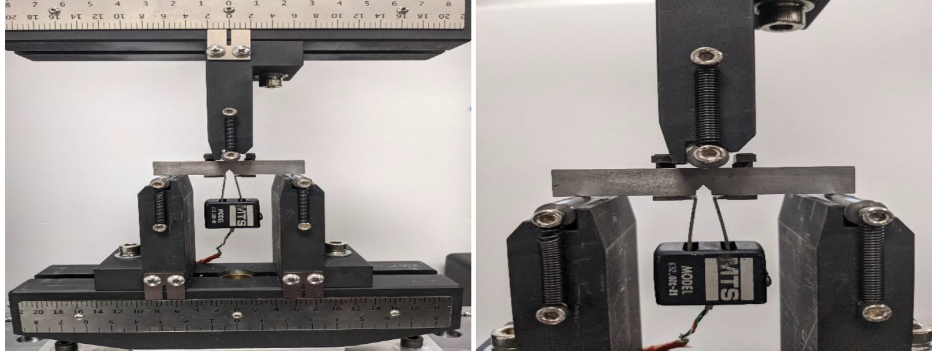


Figure 17: Experiment setup.

COD displacement response for all specimens. The straight line has 95% of the slope of the linear response. According to ASTM E399 – 20, the value at the intersection of the 95% slope and the Force - COD curve is P_Q .

Figure 19 shows an example of the determination of the crack length a . According to the standard, for each specimen, we measured the sizes $a_0 + a_1$, $a_0 + a_2$ and $a_0 + a_3$ and calculated the average of these values (a is the sum of the average value of the crack and V-notch depth 5 mm). Tables 18-19 present the fatigue fracture for both sides and the broken surface of each specimen. According to ASTM E399-20 the difference between the three different crack lengths along crack front should not exceed 10% of the average crack size. The values of a_i (where $i = 1, 2, 3$) and the differences between them are presented in Table B. Specimens 1, 6 and 10* are not within the standard specifications and are thus discarded.

It may be that during the quenching and tempering a phenomenon called “temper embrittlement” has developed in the specimens. This phenomenon cause a reduction in the toughness of steel alloys due to microstructural changes. The crack moves forward in the nuclear boundaries, so the determined fracture toughness is lower than what was expected for AISI 4340 steel alloy. All specimens are of dimensions $S = 69mm$, $B = 8mm$ and $W = 13mm$.

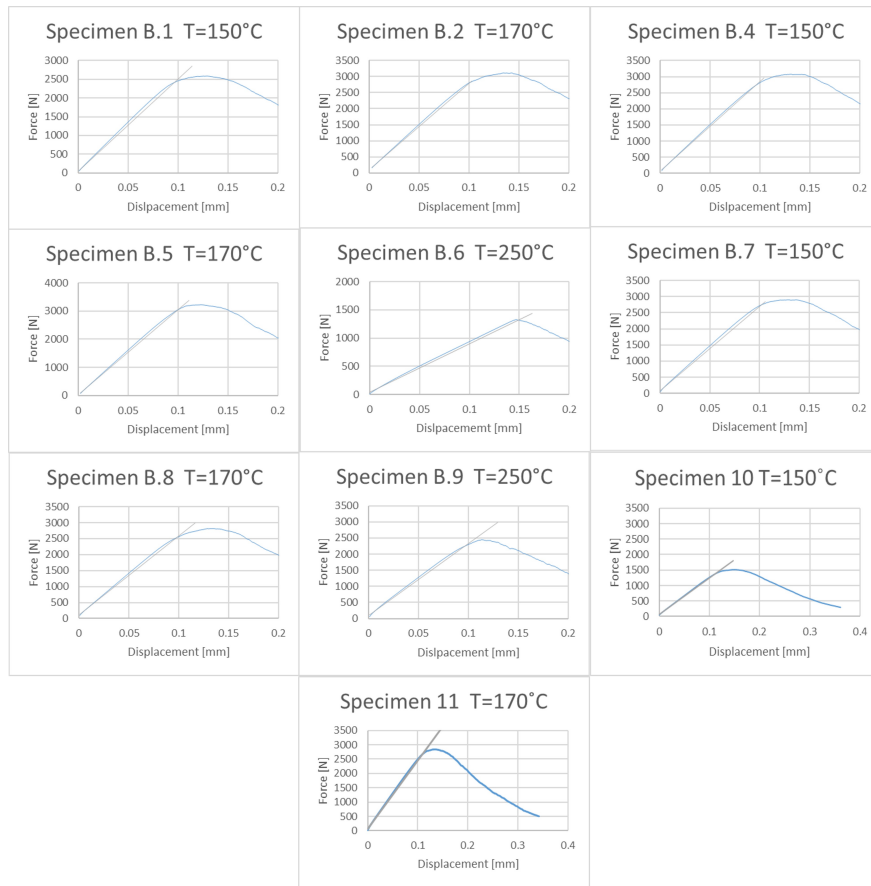


Figure 18: Force- COD displacement response for each specimen.

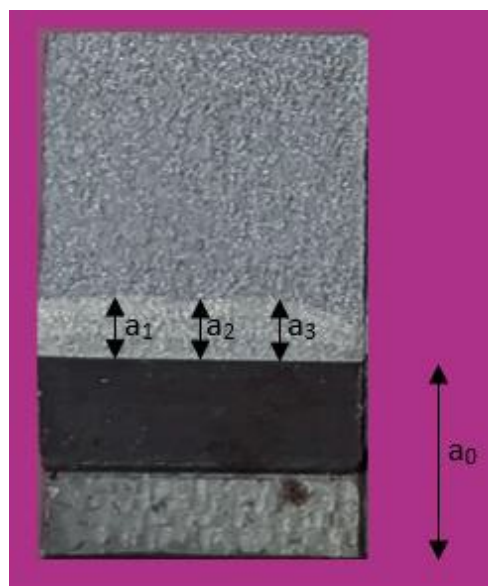


Figure 19: An example of a_i determination.

Table 17: Data of specimens for determining K_{Ic} .

Temp [°C]	Specimen	PQ [N]	a [mm]	a/W [-]	f(a/W) [-]	K_{Ic} [MPa√m]	a1 [mm]	a2 [mm]	a3 [mm]	$\frac{a1-a2}{Avg}$ %	$\frac{a1-a3}{Avg}$ %	$\frac{a2-a3}{Avg}$ %
150	1	2422	6.69	0.51	2.7928	39.36	6.98	6.8	6.3	3	10	7
	4	2759	6.54	0.50	2.6887	43.17	6.51	6.51	6.6	0	-1	-1
	7	2750	6.76	0.52	2.8372	45.40	6.56	6.76	6.95	-3	-6	-3
	10*	1436	8.50	0.65	4.7066	39.33						
	Avg (std)						44.28 (1.58)					
170	2	2770	6.73	0.52	2.8210	45.47	6.8	6.8	6.6	0	3	3
	5	3108	6.16	0.47	2.4546	44.39	6.13	6.22	6.13	-1	0	1
	8	2550	6.65	0.51	2.762	40.99	6.42	6.72	6.81	-5	-6	-1
	11*	2740	7.00	0.54	3.0204	48.16	7	7	7	0	0	0
	Avg (std)						44.75 (2.96)					
250	6	1330	8.67	0.67	4.9851	38.58	9	9	8	0	12	12
	9	2261	7.00	0.54	3.0204	39.74	7	7	7	0	0	0

* - Crack inserted by independent researcher.

Red indicates a measure not according to the standard (data of the specimen discarded).

Table 18: Specimens' fracture of $T = 150^{\circ}\text{C}$.

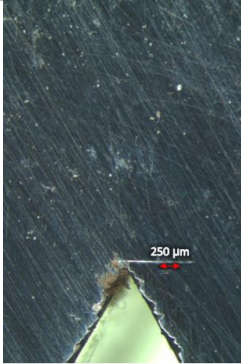
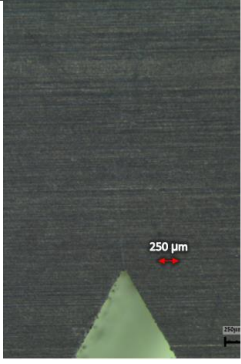
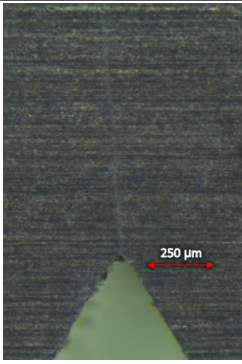
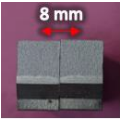
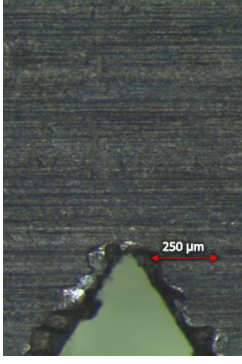
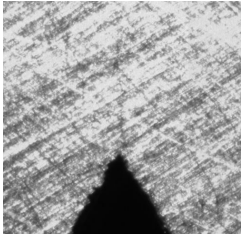
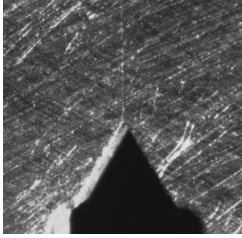
Temp [$^{\circ}\text{C}$]	Specimen #	Fatigue Fracture		Surface of broken specimens
		Side A	Side B	
150	1			
	4			
	7			
	10			

Table 19: Specimens' fracture of $T = 170^{\circ}\text{C}$.

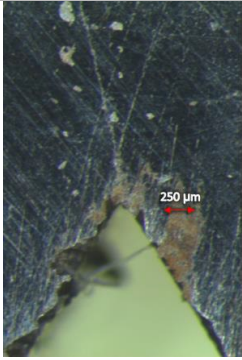
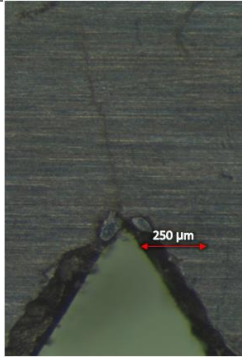
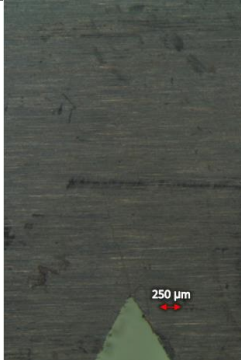
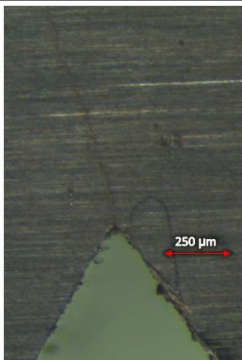
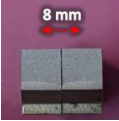
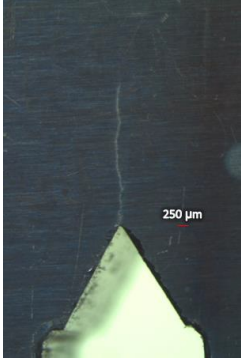
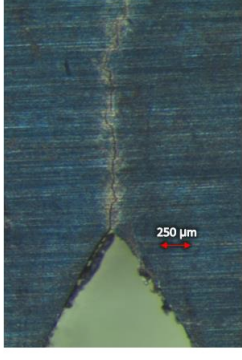
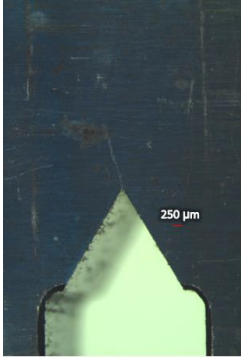
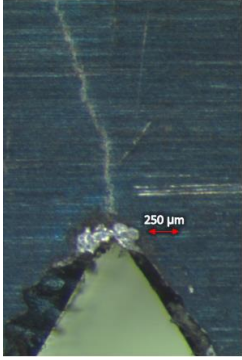
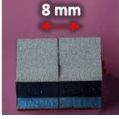
Temp [$^{\circ}\text{C}$]	Specimen #	Fatigue Fracture		Surface of broken specimens
		Side A	Side B	
170	2			
	5			
	8			
	11	Photos unavailable		

Table 20: Specimens' fracture of $T = 250^{\circ}\text{C}$.

Temp [$^{\circ}\text{C}$]	Specimen #	Fatigue Fracture		Surface of broken specimens
		Side A	Side B	
250	6			
	9			

To check the K_{Ic} value obtained, and the possibility that impurities were the reason for the lower than expected fracture toughness, we performed further K_{Ic} experiments on two specimens tempered at 150°C and 170°C , obtaining values of $38.95 \text{ MPa}\sqrt{\text{m}}$ and $42.87 \text{ MPa}\sqrt{\text{m}}$ respectively. These further experiments match well the values obtained previously, and the metallographic investigation. In Table 21 we compare K_{Ic} measured by us to these reported in [14, Table 5] for the specimens which have almost the same σ_y as our experiments. We notice a difference of almost 50% for K_{Ic} values most probably due to the impurities in our material.

Table 21: Comparison between our experiments and [14].

Current experiments			[14]	
Temp [°C]	σ_y [MPa]	K_{Ic} (STD) [MPa \sqrt{m}]	σ_y [MPa]	K_{Ic} [MPa \sqrt{m}]
150	1370	44.28 (1.58)	1400	88
170	1475	44.75 (2.96)	1469	75
250	1500	39.74 (one specimen only)	1517-1504	57-86

C V-notched specimens dimensions and load at fracture

Details on the exact dimensions of each specimen and load to fracture are tabulated in Tables 22-23. Some of the measurements were done after the specimens were broken, so there is some missing data.

Table 22: List of tested V-notched specimens, (L,H, W and Notch depth are shown in Figure 2) – angle of 30° and 60°.

V-notch angle [°]	Tempering temp [°C]	Specimen #	Force at fracture [N]	L [mm]	H [mm]	W [mm]	Notch depth [mm]
30	150	11	6698±240	80.07	10.01	10.01	5.06
		14	7896±590	80.06	10.02	10.01	5.06
		17	6644±406	80.07	9.97	10.00	5.08
		32	7113±70	-	9.93	9.99	4.96
		35	7660±370	80.22	10.05	10.02	5.06
		50	7276±110	-	10.01	9.94	4.99
		53	5641±180	-	9.96	10.00	5.06
	170	9	7506±70	-	10.02	9.99	5.04
		21	7788±146	80.07	98.98	10.02	5.04
		24	8067±722	80.15	10.00	10.00	5.09
		42	6303±82	79.97	10.01	10.02	5.10
		48	7980±760	80.20	10.02	10.03	5.11
		51	7946±330	80.15	10.04	10.01	5.10
	250	10	6445±80	80.29	10.04	10.04	4.88
		19	6706±700	80.08	10.03	10.02	5.09
		25	6403±256	80.21	10.03	10.00	5.03
		34	6756±490	80.21	10.00	10.03	5.15
		49	7665±802	80.02	10.00	9.97	5.10
52		7511±520	80.33	10.00	10.02	5.11	

60	150	1	8447±70	80.16	10.01	10.03	5.04
		13	9290±153	79.98	9.99	10.01	5.10
		16	8651±370	88.19	9.97	9.97	5.08
		19	8597±641	80.05	10.02	9.98	4.99
		22	9036±180	80.22	9.94	9.98	5.20
		25	9081±829	80.10	10.01	10.00	5.09
	170	14	8967±20	80.17	9.99	10.00	5.06
		17	9823±1000	80.12	10.01	10.02	5.04
		20	9342±501	80.06	9.99	10.01	5.07
		23	9079±716	80.08	9.97	9.98	5.03
		26	9437±669	80.04	10.01	10.02	5.10
		35	8166±470	-	10.01	10.03	5.10
	250	9	5861±40	80.05	10.01	10.02	5.04
		12	7357±300	80.27	10.03	10.00	5.06
		15	8334±160	80.31	10.01	10.01	5.05
		18	7665±450	80.16	10.01	10.03	5.07
		24	7557±90	80.29	10.02	10.05	5.17
		30	7931±807	80.07	10.00	10.03	5.10

Table 23: Continued list of tested V-notched specimens, (L,H, W and Notch depth are shown in Figure 2) – angle of 90°.

V-notch angle [°]	Tempering temp [°C]	Specimen #	Force at fracture [N]	L [mm]	H [mm]	W [mm]	Notch depth [mm]
90	150	19	11789±1134	80.25	9.99	9.95	5.03
		22	11480±511	80.08	10.01	10.01	5.06
		34	12855±1135	80.05	10.00	9.99	5.08
		43	9376±70	80.14	9.99	10.03	5.03
		46	13683±240	80.40	9.95	9.95	5.02
		52	9836±420	80.23	9.94	9.97	5.05
	170	23	14204±1250	80.28	9.99	10.01	5.05
		26	15163±1364	80.16	9.98	9.98	5.08
		29	12293±253	80.26	9.98	9.98	5.09
		35	12550±50	80.16	10.01	10.01	5.16
		47	12659±1106	79.98	10.02	9.98	5.02
		56	12521±190	80.35	10.02	10.02	5.05
	250	3	8779±80	80.26	9.99	10.02	5.09
		21	10947±730	80.16	10.03	10.01	5.11
		24	11024±480	80.10	10.03	10.02	5.05
		36	11534±480	80.43	10.00	10.02	5.11
		39	10298±810	80.17	10.02	10.02	5.06
		42	9413±362	80.10	10.02	9.99	5.09

All broken V-notched specimens are shown in Figure 20.



Figure 20: Broken V-notched specimens. In the bottom photo: only the upper specimens are fractured.

D Measurements of notch-tip radius

To quantify the notch tip radius we measured it by a microscope. For each V-notch angle we measured the tip radius of the first and last specimens. The specimen's photos are presented in Tables 24 - 25. The notch radii range are presented in Table 26.

Table 24: Notch tip diameter measurements in μm – part 1

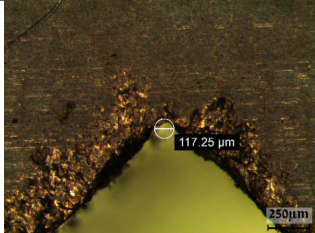
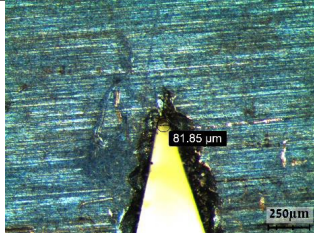
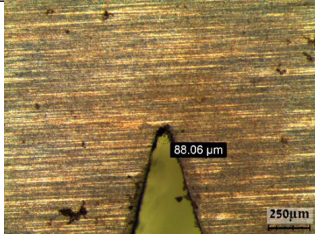
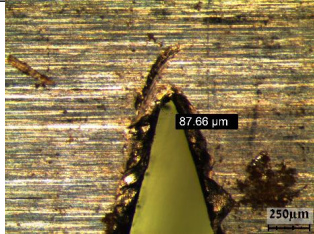
V-notch angle [°]	Specimen #	Side A	Side B
30	1		
	54		

Table 25: Notch tip diameter measurements in μm – part 2.

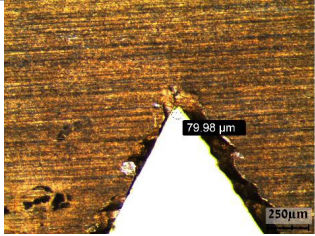
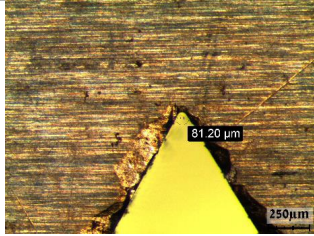
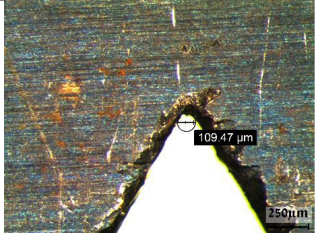
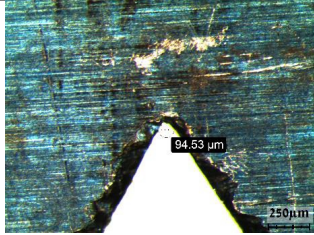
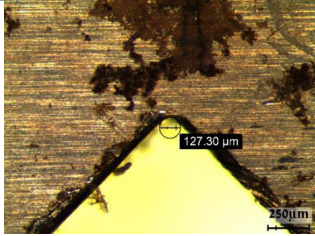
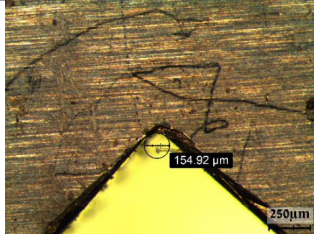
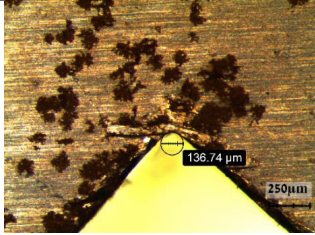
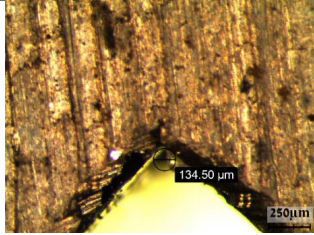
V-notch angle [°]	Specimen #	Side A	Side B
60	2		
	36		
90	1		
	55		

Table 26: Notch radii range [μm]

V-notch angle [$^{\circ}$]	Notch radii range μm
30	35-44
60	40-55
90	64-77

E Determining plastic zone by DIC

The area sizes determined by the DIC and by the FEA for all specimens are detailed in Tables 36-38. Small PZ means the plastic zone area is too small compared to the threshold area. Area which cannot be determined means there was a big uncertainty about where exactly the plastic zone is.

Table 27: Plastic zone as determined by DIC with $T = 150^\circ$ and $\omega = 30^\circ$.

$T = 150^\circ, \omega = 30^\circ$					
Scale	Specimen	$v = 0.3$		$v = 0.5$	
		$\varepsilon_y = 0.83\%$	$\varepsilon_y = 0.93\%$	$\varepsilon_y = 0.83\%$	$\varepsilon_y = 0.93\%$
	11				
	14				
	17				
	32				
	35				
	50				

Table 28: Plastic zone as determined by DIC with $T = 150^\circ$ and $\omega = 60^\circ$

$T = 150^\circ, \omega = 60^\circ$					
Scale	Specimen	$\nu = 0.3$		$\nu = 0.5$	
		$\varepsilon_y = 0.83\%$	$\varepsilon_y = 0.93\%$	$\varepsilon_y = 0.83\%$	$\varepsilon_y = 0.93\%$
	1				
	13				
	16				
	19				
	22				
	25				

Table 29: Plastic zone as determined by DIC with $T = 150^\circ$ and $\omega = 90^\circ$.

$T = 150^\circ, \omega = 90^\circ$					
Scale	Specimen	$\nu = 0.3$		$\nu = 0.5$	
		$\varepsilon_y = 0.83\%$	$\varepsilon_y = 0.93\%$	$\varepsilon_y = 0.83\%$	$\varepsilon_y = 0.93\%$
	19				
	22				
	34				
	43				
	46				
	52				

Table 30: Plastic zone as determined by DIC with $T = 170^\circ$ and $\omega = 30^\circ$.

$T = 170^\circ, \omega = 30^\circ$					
Scale	Specimen	$\nu = 0.3$		$\nu = 0.5$	
		$\varepsilon_y = 0.95\%$	$\varepsilon_y = 1\%$	$\varepsilon_y = 0.95\%$	$\varepsilon_y = 1\%$
	9				
	21				
	24				
	42				
	48				
	51				

Table 31: Plastic zone as determined by DIC with $T = 170^\circ$ and $\omega = 60^\circ$.

$T = 170^\circ, \omega = 60^\circ$					
Scale	Specimen	$\nu = 0.3$		$\nu = 0.5$	
		$\varepsilon_y = 0.95\%$	$\varepsilon_y = 1\%$	$\varepsilon_y = 0.95\%$	$\varepsilon_y = 1\%$
	14				
	17				
	20				
	23				
	26				
	35				

Table 32: Plastic zone as determined by DIC with $T = 170^\circ$ and $\omega = 90^\circ$.

$T = 170^\circ, \omega = 90^\circ$					
Scale	Specimen	$\nu = 0.3$		$\nu = 0.5$	
		$\varepsilon_y = 0.95\%$	$\varepsilon_y = 1\%$	$\varepsilon_y = 0.95\%$	$\varepsilon_y = 1\%$
	23				
	26				
	29				
	35				
	47				
	56				

Table 33: Plastic zone as determined by DIC with $T = 250^\circ$ and $\omega = 30^\circ$.

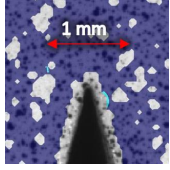
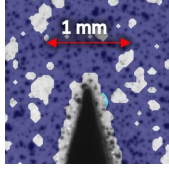
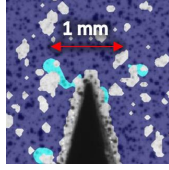
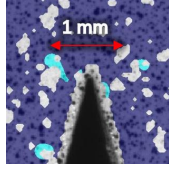
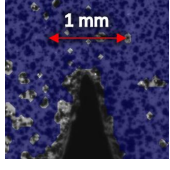
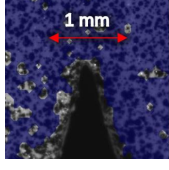
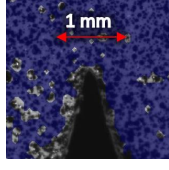
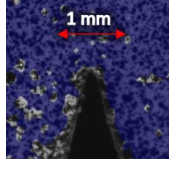
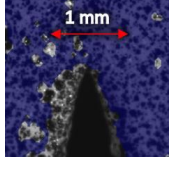
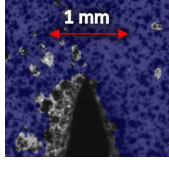
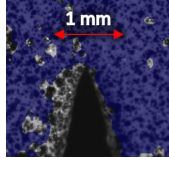
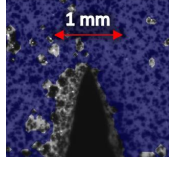
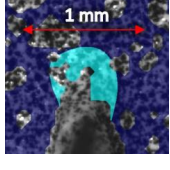
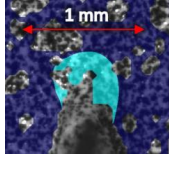
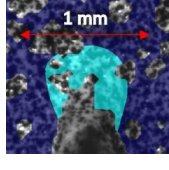
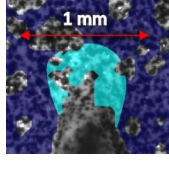
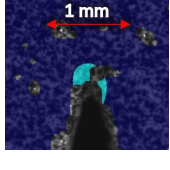
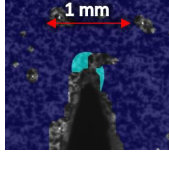
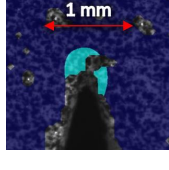
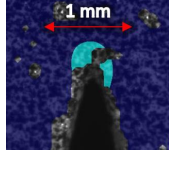
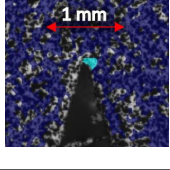
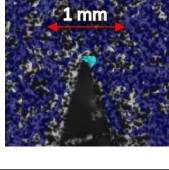
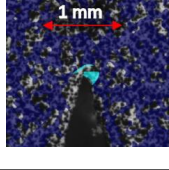
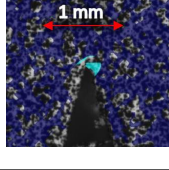
$T = 250^\circ, \omega = 30^\circ$					
Scale	Specimen	$\nu = 0.3$		$\nu = 0.5$	
		$\varepsilon_y = 0.95\%$	$\varepsilon_y = 0.98\%$	$\varepsilon_y = 0.95\%$	$\varepsilon_y = 0.98\%$
	10				
	19				
	25				
	34				
	49				
	52				

Table 34: Plastic zone as determined by DIC with $T = 250^\circ$ and $\omega = 60^\circ$.

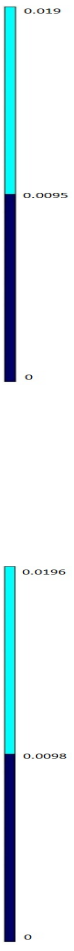
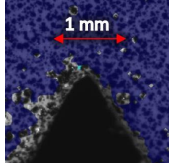
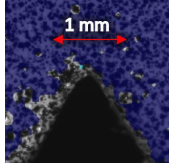
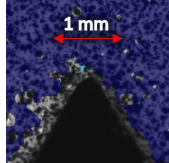
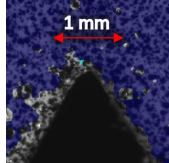
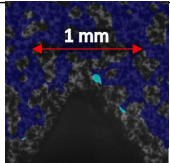
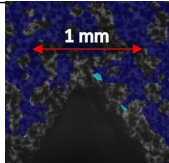
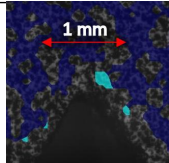
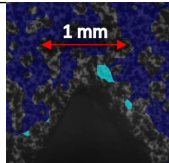
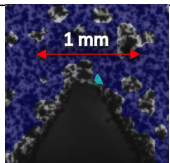
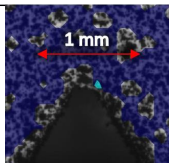
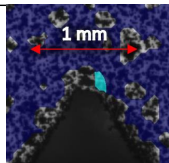
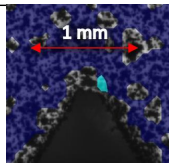
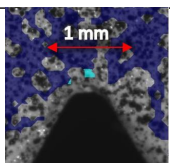
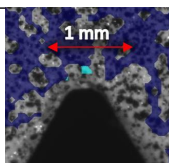
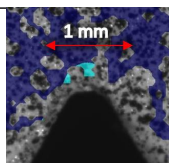
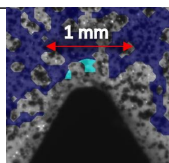
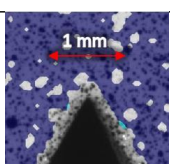
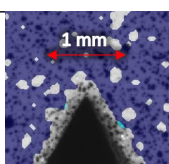
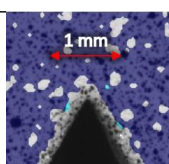
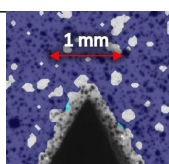
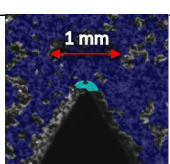
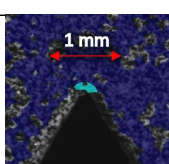
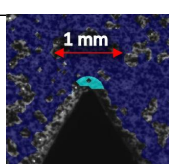
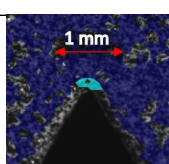
$T = 250^\circ, \omega = 60^\circ$					
Scale	Specimen	$\nu = 0.3$		$\nu = 0.5$	
		$\varepsilon_y = 0.95\%$	$\varepsilon_y = 0.98\%$	$\varepsilon_y = 0.95\%$	$\varepsilon_y = 0.98\%$
	9				
	12				
	15				
	18				
	24				
	30				

Table 35: Plastic zone as determined by DIC with $T = 250^\circ$ and $\omega = 90^\circ$.

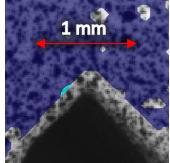
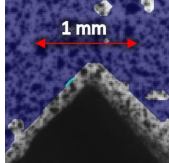
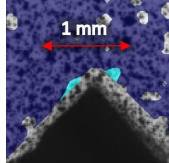
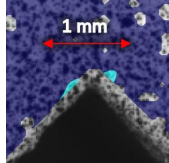
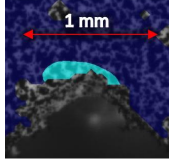
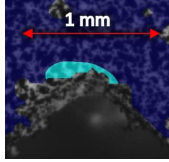
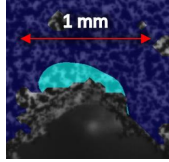
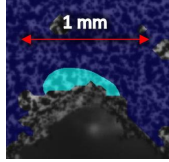
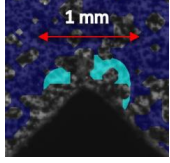
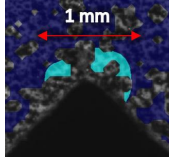
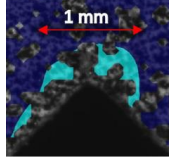
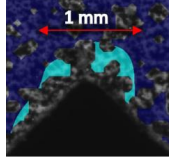
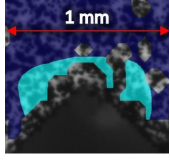
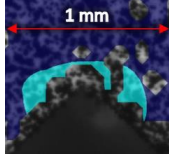
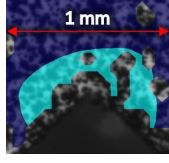
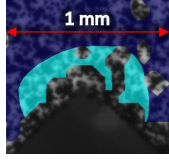
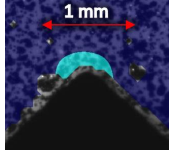
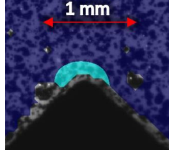
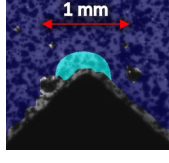
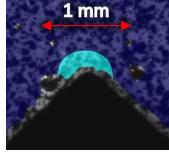
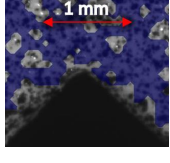
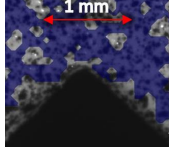
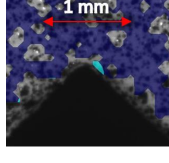
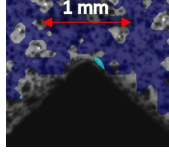
$T = 250^\circ, \omega = 90^\circ$					
Scale	Specimen	$\nu = 0.3$		$\nu = 0.5$	
		$\varepsilon_y = 0.95\%$	$\varepsilon_y = 0.98\%$	$\varepsilon_y = 0.95\%$	$\varepsilon_y = 0.98\%$
	3				
	21				
	24				
	36				
	39				
	42				

Table 36: Comparison of measured and computed plastic zone areas $T = 150^\circ$.

Tempering temperature [°C]	ω [°]	Specimen #	DIC - Area [mm ²]		SC -Area [mm ²]
			$\nu = 0.3$	$\nu = 0.5$	
150 $\varepsilon_y = 0.93\%$ $\sigma_y = 1370$	30	11	0	0.05	0.16±0.02
		14	0.16	0.20	0.305±0.075
		17	0	0	0.165±0.035
		32	cannot be determined	cannot be determined	0.205±0.005
		35	0.01	0.09	0.265±0.045
		50	0.26	0.34	0.22±0.01
		53	None	None	0.09±0.01
	60	1	0.23	0.34	0.38±0.01
		13	0.17	0.23	0.54±0.03
		16	0.07	0.11	0.415±0.065
		19	0.11	0.14	0.415±0.105
		22	0.04	0.07	0.48±0.03
		25	0.10	0.17	0.505±0.155
	90	19	0.42	0.52	1.405±0.455
		22	0.34	0.41	1.25±0.19
		34	0.59	0.78	1.87±0.54
		43	0.13	0.31	0.6±0.02
		46	0.88	1.13	2.24±0.12
		52	0.13	0.21	0.72±0.11

Table 37: Comparison of measured and computed plastic zone areas, $T = 170^\circ$.

Tempering temperature [°C]	ω [°]	Specimen #	DIC - Area [mm ²]		SC -Area [mm ²]
			$\nu = 0.3$	$\nu = 0.5$	
170 $\varepsilon_y = 0.95\%$ $\sigma_y = 1440$	30	9	small PZ	small PZ	0.21
		21	0.12	0.13	0.25
		24	0.18	0.22	0.36
		42	0.28	0.35	0.12
		48	0.37	0.40	0.35
		51	0	0	0.29
	60	14	0.14	0.14	0.39
		17	0.14	0.17	0.75
		20	small PZ	0.10	0.55
		23	0.13	0.15	0.54
		26	0	0	0.61
		35	0.03	0.04	0.34
	90	23	0.98	1.03	2.8
		26	1.22	1.47	3.49
		29	0.55	0.72	1.43
		35	0.63	0.77	1.45
		47	0.46	0.57	1.93
		56	0.42	0.46	1.49

170 $\varepsilon_y = 1\%$ $\sigma_y = 1510$	30	9	small PZ	small PZ	0.17
		21	0.10	0.10	0.18
		24	0.13	0.20	0.16
		42	0.28	0.31	0.09
		48	0.34	0.41	0.15
		51	0	0	0.19
	60	14	0.10	0.18	0.33
		17	0.11	0.18	0.32
		20	0	0.08	0.32
		23	0.10	0.15	0.26
		26	0	0	0.31
		35	0.03	0.04	0.19
	90	23	0.89	1.17	1.34
		26	1.02	1.31	1.66
		29	0.47	0.59	1.04
		35	0.52	1.17	1.2
		47	0.41	0.49	0.9
		56	0.34	0.54	1.14

Table 38: Comparison of measured and computed plastic zone areas, $T = 250^\circ$

Tempering temperature [°C]	ω [°]	Specimen #	DIC - Area [mm ²]		SC -Area [mm ²]
			$\nu = 0.3$	$\nu = 0.5$	

<p>250</p> <p>$\varepsilon_y = 0.98\%$</p> <p>$\sigma_y = 1500$</p>	30	10	small PZ	small PZ	0.105±0.005
		19	0	0	0.125±0.045
		25	0	0	0.105±0.015
		34	0.18	0.24	0.125±0.035
		49	0.13	0.19	0.205±0.075
		52	0.02	0.05	0.185±0.045
	60	9	small PZ	small PZ	0.07
		12	small PZ	small PZ	0.165±0.025
		15	small PZ	small PZ	0.26±0.02
		18	0.08	0.12	0.195±0.045
		24	small PZ	small PZ	0.18±0.01
		30	0.04	0.07	0.235±0.085
	90	3	small PZ	0.13	0.33±0.01
		21	0.10	0.16	0.765±0.175
		24	0.32	0.40	0.785±0.125
		36	0.19	0.27	0.92±0.14
		39	0.13	0.16	0.625±0.175
		42	small PZ	small PZ	0.435±0.065